The International Journal of Advanced Manufacturing Technology (2025) 139:631–656
https://doi.org/10.1007/s00170-025-15901-4

ORIGINAL ARTICLE

A comparative investigation on microstructural, mechanical, and corrosion behavior of friction stir processed surface composite of magnesium alloy reinforced with nanoparticles

Surendra Kumar Patel[1] · Guoxin Dai[1] · Lei Shi[1] · Chuansong Wu[1] · Sergey Mironov[2] · Lei Guan[3]

Received: 17 September 2024 / Accepted: 4 June 2025 / Published online: 16 June 2025

Abstract

Magnesium and its alloys have been well known for human implant applications due to their similar structural and mechanical properties to bone and biodegradability. The aim of this research work was to investigate the comparative microstructural, microhardness, tensile, and corrosion properties of the nanoparticle-reinforced AZ91D alloy surface composites fabricated by the friction stir processing method for human implants. The FSP surface composites were fabricated with 15 wt.% reinforced with hydroxyapatite ($Ca_5(PO_4)_3(OH)$, as called HA), ZrO_2, and Y_2O_3 nanoparticles into the AZ91D alloy at one, two, and three passes. The reinforcements were filled into the AZ91D alloy surface using the holes method; after that, surface processing was carried out with a 2.5° tilt angle, 800 rpm rotation, and 80 mm/min tool traverse speed. The microstructural changes were observed on the equal distribution of reinforcements and grain refinement into the processed surface matrix, which was analyzed by OM, SEM, EBSD, XRD, and EDS analysis. The average grain size in the processed surface was reduced by 2.5 μm, 3.1 μm, and 2.7 μm for Y_2O_3, HA, and ZrO_2 incorporation at three passes. The microhardness and tensile strength of the AZ91D/ZrO_2 composite were increased compared to the AZ91D/Y_2O_3 and AZ91D/HA composites at three passes due to increased nano-sized precipitation and the generation of a non-basal slip system due to dynamic recrystallization. The corrosion resistance of the processed surface was investigated through the immersion method using simulated body fluid (SBF). The corrosion resistance of the processed surface was increased with the increasing number of days due to an optimal beneficial effect of forming passive layers that chemically react with SBF fluid. However, the AZ91D/ZrO_2 composite shows better corrosion resistance compared to the AZ91D/Y_2O_3 and AZ91D/HA composites due to increased chemically stable passive phase layers forming over the surface.

Keywords Friction stir processing · Nanoparticle-reinforced surface composite · Magnesium alloy · Microstructural evolution · Corrosion behavior

1 Introduction

Magnesium material and its alloys are quite interesting for metallic implant material for their better bio-dissolving characteristics and excellent capability to absorb the adjoining physiological behavior into human body fluid [1]. Moreover, a magnesium ion constituent is highly prolific in citation into the biological environment and very helpful for biological implementation [2]. Approximately 60% of the overall physiological Mg constituents are stored in the human body during bone tissue implants. The unadventurous implant materials, for example, Ti-, Ca-, P-, Zr-, and Y-based alloys may release toxic ions, leading to reactions with the physiological environment. As a result, the majority of Mg concentrations can be used in implants to promote

✉ Lei Shi
lei.shi@sdu.edu.cn

[1] MOE Key Lab for Liquid-Solid Structure Evolution and Materials Processing, Shandong University, Jinan 250061, China

[2] Laboratory of Mechanical Properties of Nanoscale Materials and Superalloys, Belgorod National Research University, 308015 Belgorod, Russia

[3] State Key Laboratory of Precision Electronic Manufacturing Technology and Equipment, Guangdong University of Technology, Guangzhou 510006, People's Republic of China

tissue regeneration and the formation of biological apatite [3]. Mg alloys may pose a toxicity risk due to the alloying element that causes β-amyloid peptide aggregation in tissue, resulting in pathological lesions in Alzheimer's illness [4]. Thus, selecting biologically compatible alloying materials is crucial in maintaining the influence of bone characteristics [5]. Furthermore, the biodegradable nature of Mg-based alloy implants eliminates the need for surgical removal of the utilized implants prior to healing, saving recovery time and associated expenses [6].

Furthermore, due to its unique blend of biodegradable and mechanical behavior, Mg-alloy is a promising option to biomedical grade metallic biomaterials for temporary load bearing application for scaffold [7]. Although, ceramic alloying elements possess increased biodegradable characteristics and reduced mechanical strength for load bearing applications [8]. But added secondary ceramic alloying into Mg-alloy through conventional methods produces stiffer and denser temporary bone than human bone and are more suitable for desired load bearing applications [9]. Also, the hybrid joint efficiency such as ultimate tensile strength, yield strength, and percentage elongation are increased using the parameters for both welding methods DS-FSW and SS-FSW [10, 11]. A few researchers investigated the crucial role of fundamental mechanical characteristics like yield strength, ductility and hardness in controlled plastic deformation during FSW/FSP [12]. A similar observation extended to Mg-based composite fabricated through FSP technique, where those with lower yield strength, reduced hardness and greater ductility shows enhanced processibility for human implants Mg-based materials (such as AZ91, AZ31, ZE41, ZK60, AZ61, ZKX60, and WE43 alloy) with incorporation of boa-active nanoparticles [13–17]. Yet, ahead implantation, due to modulus disparity and surrounding stress shielding effect into the bone tissue may affect the reduction in bone density and new cell growth in turn of time respectively. In contrast, the young's modules and density of mg and its alloys is approximate (45–50) GPa and 1.72 g/cm^3 correspondingly, which is similar to the natural human bone [18].

In spite of the recompense appliances magnesium and its alloys are the primary challenges in implementation as human surgical components due to their inadequate oxidation resistance in physiological environment [19]. The magnesium surface is naturally prone to numerous electrochemical processes with unstable chemical species of sodium chloride in blood which is attributed to rapid oxidation behavior. The subsequent corrosion occurs during chemical reduction. Firstly, there is a swift evolution of hydrogen content which causes challenges in the chemical reaction of bone cell attachment (e.g., $Mg_{(s)} + 2H_2O \rightarrow Mg(OH)_2 + H_2$)) [20–23]. The second one assesses how much the implants structural reliability has decreased. Therefore, the challenge is that the low corrosion rate of the Mg-based alloy allows it to fulfill its intended function for an extended duration while the damaged tissue undergoes healing or repairs [24]. Additionally, it has been noted that magnesium hydroxide ($Mg(OH)_2$) and oxide (MgO) are primary components that cause corrosion in Mg materials. ($Mg(OH)_2$) typically function as a passive phase layer to mitigate the effect of a damp environment [25]. However, the blinking activity of the ($Mg(OH)_2$) layer is unable to protect corrosion rates in biological nature. Furthermore, it is extremely susceptible to react with Cl^- ions to form surface dispersed, highly soluble $MgCl_2$ compounds [26]. The incorporated biological particles in magnesium matrix are enhancing the micro galvanic corrosion resistance in biological bodily fluid. Also, Mg-based alloys are mostly affected by formed impurities and secondary metallic phase in micro galvanic reactions because of its lower electrochemical potential, which resulted in increased deep micro cuts and pitting behavior [27].

During FSP, significant changes in corrosion behavior may arise based on the processing conditions. Three elements can influence corrosion behavior and consequently either worsen or improve corrosion resistance [28]. Although large micro constituents and residual stresses negatively impact corrosion behavior, grain refinement positively influences it. These three factors often compete with one another to influence corrosion behavior [29]. This research demonstrates that grain size plays a crucial role, as all the Mg-based FSP composites exhibited enhanced corrosion resistance. Nonetheless, it is possible that certain electrochemical outcomes may lack a significant relationship with FSP conditions [30]. FSP conditions can enhance or diminish the influence of the three factors, though their interrelation is complex, and further in-depth research studies are still necessary.

In the direction of resolving these problems, much research employs a variety of technological strategies, including surface altering, synthesis of bulk composite and coating to enhance biological corrosion resistance. Up to now, FSP has been mostly used by several researchers for improving the microstructural, mechanical and corrosion properties of the Mg-based surface composite and there has been limited research studies carried out for successful biocompatible implants. Thus, this study was conducted addressing the research gap concerning the comparative analysis of bioactive-reinforced Mg surface composites produced using the FSP method. Hence, the current work is investigated on comparative studies on fabrication of yttrium oxide (Y_2O_3)-, hydroxyapatite (HA)-, and zirconium oxide (ZrO_2)-reinforced AZ91D surface composite fabricated by FSP technique. Being dominant constituents, Y_2O_3, HA and ZrO_2 have been considered as the most reactive bioactive ceramics element for orthopedic implants. The presence of ceramic nanoparticles inside the implants surface matrix usually increases the

apatite matrix layers for enhanced extra bone cell attraction to the implants bone recovery as well as repair [31]. Also, the generated apatite layer must provide better AZ91D surface protection to corrosion for a long time after implantation. In addition, the various biological entities of Y_2O_3, HA and ZrO_2 nanoparticles could help in the generation of osteosarcoma and attachment of various grain sizes into implants. Additionally, the solubility of the added nanoparticles is much closer to natural body fluid in the implant.

2 Experimental procedure

2.1 Used materials

Commercially available AZ91D alloy plate (with chemical composition, 8.3 wt% Al, 1 wt% Zn, 0.5 wt% Mn, 0.03 wt% Cu, and Mg balance) of size 300 mm length × 60 mm width × 5 mm thickness were used for fabricating surface composite. The valid reason has been explained by the current research group for AZ91D alloy. The 99.9% pure Y_2O_3-, HA-, and ZrO_2-reinforced nanoparticle size (50 nm) with 15 weight percentage were used to fabricate AZ91D alloy surface composite for investigation. The reinforcement particles mixed with nanoparticles were filled into an AZ91D alloy plate using 2 mm diameter and 3.5 mm length holes as shown in Fig. 1a. Furthermore FSP processing was performed.

2.2 Fabrication of surface composite through FSP

The FSP was performed to ensure proper dispersion of incorporated reinforced nanoparticles into the AZ91D alloy matrix with solid state technique. The FSP tool was made of H-13 steel with a left hand thread tapered conical pin (12.3 mm solder diameter, 6 mm pin root diameter, 5 mm pin tip diameter, and 3.9 mm threaded in length) as shown in Fig. 1b and f. The tool rotational speed of 800 rpm and traverse speed of 80 mm/min were used for fabricating the surface composite. Also, the tool tilt angle of 2.5° was constant during multi-pass FSP. These processing parameters were optimized after many primary trials to achieve the effective dispersion of additive particles and smooth fabrication of AZ91D surface composite. For equal distribution of Y_2O_3, HA, and ZrO_2 nanoparticles into the AZ91D alloy matrix, each tool pass was started from the previous original starting point with 100% overlap as shown in Fig. 1c and d. The FSP passes were repeated three times to ensure the equal dispersion of the reinforcement nanoparticle into the AZ91D alloy matrix.

2.3 Phase identification

The generated phases in the FSP AZ91D alloy surface with additive particles were observed using X-ray diffraction (XRD) employing an X-ray diffractometer with CuKα radiation (0.15-nm wavelength). The XRD analysis was operated at 44 mA and 40 kV in 2θ range of 10–70° using a step size

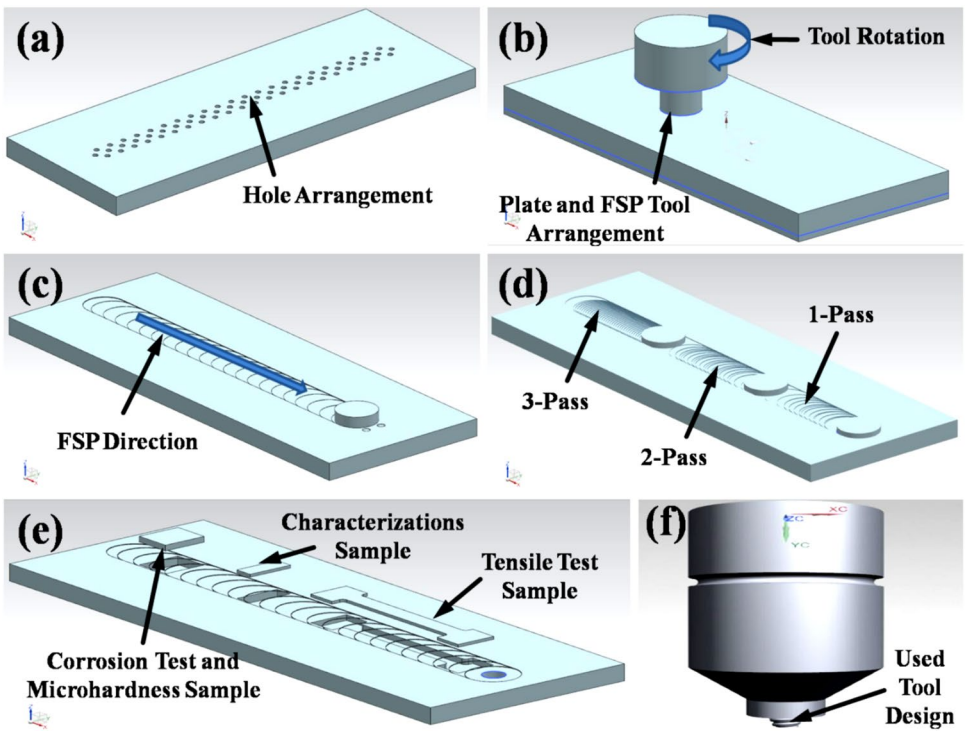

Fig. 1 Schematic of the experimental procedure. **a** arrangement of holes; **b** plate and tool arrangement; **c** FSP direction; **d** one, two, and three FSP passes; **e** sample preparation; and **f** tool design

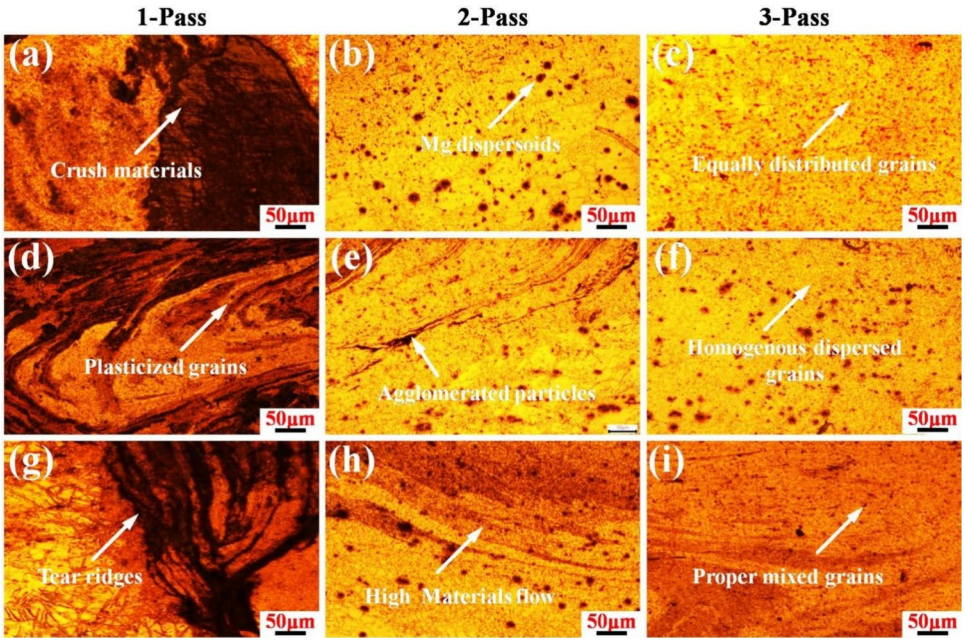

Fig. 2 Optical images of AZ91D/Y_2O_3 at **a** 1 pass, **b** 2 passes, and **c** 3 passes; AZ91D/HA at **d** one pass, **e** two passes, and **f** three passes; and AZ91D/ZrO_2 FSP surface composite at **g** one pass, **h** two passes, and **i** three passes

of 0.025° and a scan rate of 10°/min. The phase identification of the XRD sample was analyzed by JADE-6 software with cam paired with the standard international center for diffraction data (ICDD), the data obtained from the joint committee of powder standard (JCPDS).

2.4 Mechanical test and microstructure evaluation

The microhardness was performed on HVS-1000Z tester with gradually applying constant load 200 N for 10 s. And tensile specimens were cut along the processing direction (Fig. 1e), and the tensile test was performed at room

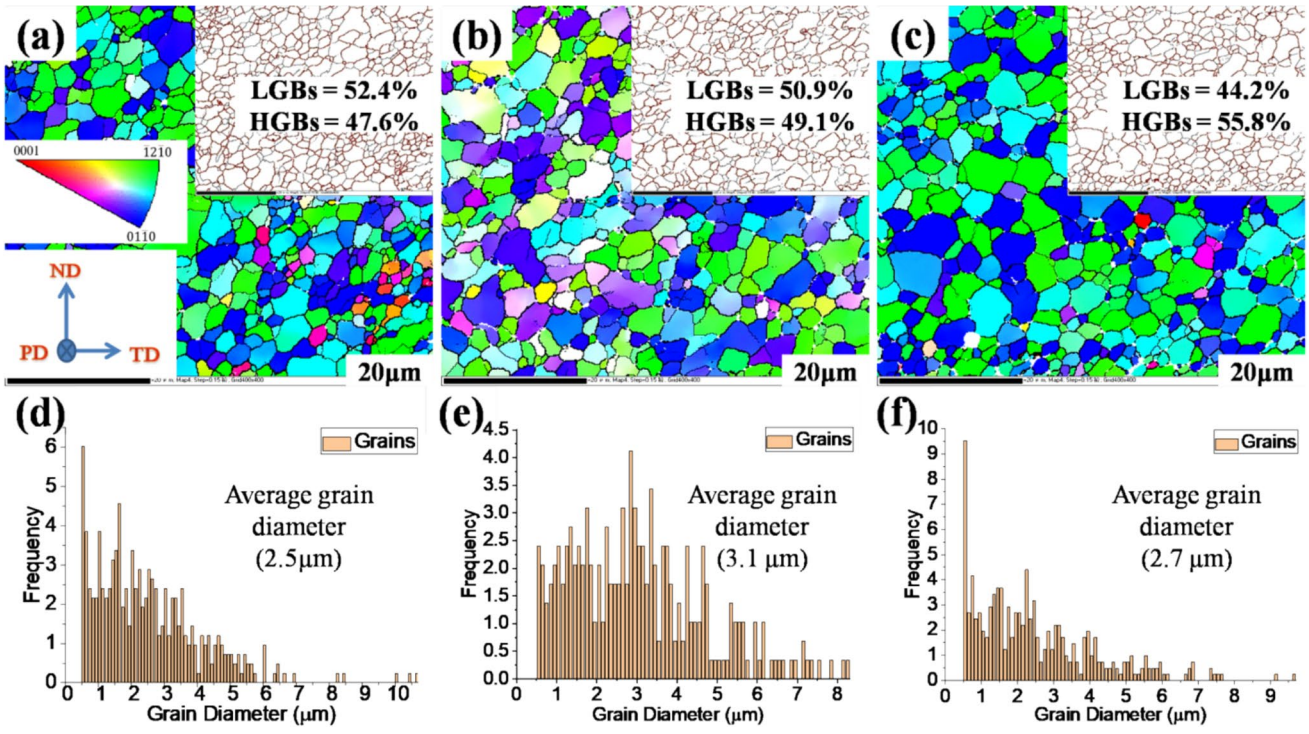

Fig. 3 EBSD image of the FSP surface composite at three passes: **a** AZ91D/Y_2O_3, **b** AZ91D/HA, and **c** AZ91D/ZrO_2; **d** corresponding grain diameter of (**a**); **e** corresponding grain diameter of (**b**); and **f** corresponding grain diameter of (**c**)

temperature on WDW-100AE equipment after polished the rough surface. The dimensions of the microhardness and tensile test samples were designed according to the ISO 6892–1:2009 standard. The strain rate was 1.0×10^{-3} s^{-1}. In order to ensure the accuracy of data, each group of samples was tested three times. The microstructure analysis and reinforced particles distribution into the stir zone of reinforced AZ91D surface were investigated through optical microscope (OM), scanning electron microscope (SEM) equipped with Energy Dispersive X-ray Spectroscopy (EDS) and electron back scattered diffractometer (EBSD). The channel-5 image processing software was used for surface texture analysis with EBSD raw data of the FSP surface composites. The samples for microstructure characteristics were cut by using a wire EDM machine as shown in Fig. 1e. The FSP samples and substrate AZ91D alloy were molded in epoxy followed by mechanical polishing with different grain sizes (600–2000 µm) of SiC paper. After that samples were polished on 2500-µm SiC paper with continuous flow of water. Furthermore the rough ground samples surface were polished by impregnated buehler cloth with diamond pest (particle size 2 to 0.5 µm) to get scratch free surface. The proper polished samples were ultrasonically cleaned with methanol for 5 min. To see the clear microstructure behavior of FSP composite and AZ91D alloy samples were etched in the mixed chemicals (with chemical compositions: water (10 mL) + nitric acid (3 mL) + 3 g malic acid (3 g)) to immersion etching for 7 min.

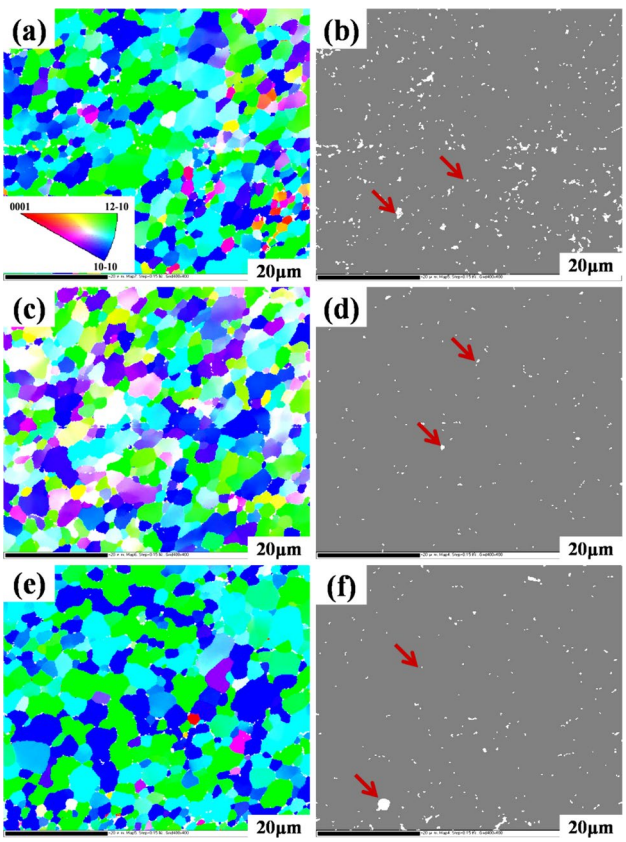

Fig. 4 EBSD images with EDS counts of FSP surface composite at three passes: **a** AZ91D/Y_2O_3 and **b** its corresponding EDS, **c** AZ91D/HA and **d** its corresponding EDS; and **e** AZ91D/ZrO_2 and **f** its corresponding EDS

2.5 Corrosion test evaluation

The corrosion test was performed using a normalized weight loss measurement method. Before using the samples for the corrosion test, all samples were cleaned of the dirt or foreign matter from the surface of the samples. Clean the specimen with a solvent or cleaner and dry to remove all the traces of the solvent; FSP samples with residual magnetism should be demagnetized before use. The entire test samples were polished using a 2000-µm SiC paper, followed by ultrasonic cleaning with methanol for 3 min before performing the corrosion test. During the test, SBF temperature was maintained at 35°, as per normal human body temperature. The corrosion test was performed on FSP and substrate materials in fractions of 7 days, 15 days, and 30 days, respectively, as per G31-72(2004) standard. Furthermore, the test resulted in five mass loss values corresponding to the average mass loss values obtained for the accuracy of results. The mass loss was calculated by using Eq. (1).

$$Weight\ loss\ in\ mm^3 = \frac{weight\ loss\ in\ gms\ \times\ 1000}{original\ weight\ of\ sample} \quad (1)$$

The mass loss was calculated using a weighing machine with the accuracy of 0.0001 g. To understand the long-term corrosion behavior, the worn features of the FSP samples were observed by SEM analysis. Also, the corroded samples were dried at 60° temperature for 24 h to remove the complete moisture from the samples.

3 Results and discussion

3.1 Microstructure evaluation

The optical microstructure shows the comparative study of the AZ91D/Y_2O_3, AZ91D/HA and AZ91D/ZrO_2 surface composite as shown in Fig. 2a–i. The 1-pass samples hold major deficiencies that were disastrous in beginning inspections, so it cannot be considered for further characterizations in depth. The microstructure of the FSP samples is affected by various factors, including plasticized strain rate, strains and processing temperature. During the reinforced FSP process, the reinforced particles and temperature affect the grain growth into the matrix [32]. Thus, the disparity in the grains nucleation rate developed by FSP temperature throughout

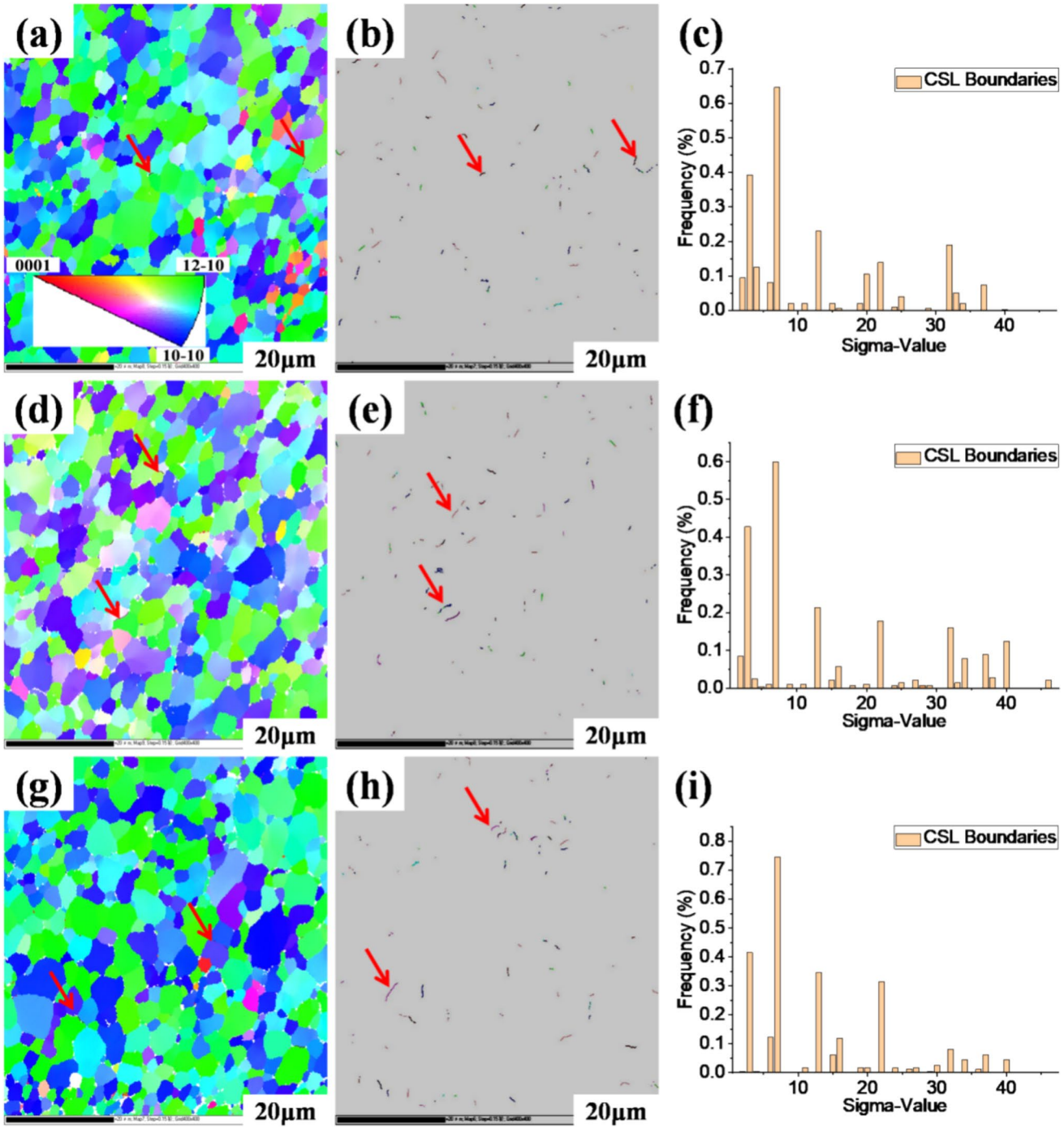

Fig. 5 EBSD image of CSL boundary of FSP surface composite at three passes **a** AZ91D/Y_2O_3 composite and **b** and **c** its corresponding CSL boundary representation and sigma value of plane orientations, **d** AZ91D/HA composite and **e** and **f** its corresponding CSL boundary representation and sigma value of plane orientations, and **g** AZ91D/ZrO_2 composite and **h** and **i** its corresponding CSL boundary representation and sigma value of plane orientations

the nucleation stage is important. The frictional heat generation and high strain rate in the processed zone showed better DRX which resulted in the proper flow of materials and distribution of reinforcement particles [33]. Hence, FSP passes enhanced the material flow and increased the homogeneous distribution of reinforcement particles into the FSP zone.

It is revealed that with increased pass, the grain size of the reinforced FSPed AZ91D/Y_2O_3 (Fig. 2c), AZ91D/HA

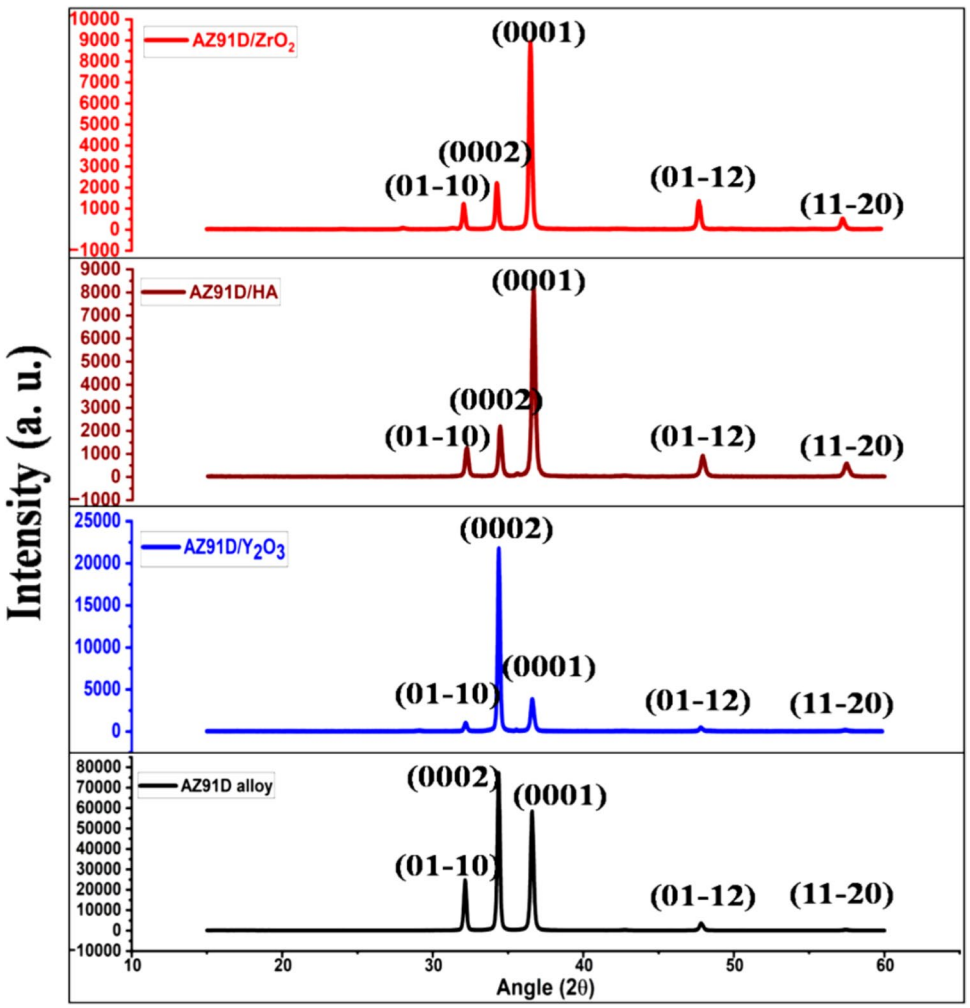

Fig. 6 XRD image of AZ91D alloy, AZ91D/Y_2O_3, AZ91D/HA, and AZ91D/ZrO_2 FSP surface composite at three passes

(Fig. 2f), and AZ91D/ZrO_2 (Fig. 2i) composite reduced due to the improved shear deformation, which occurs by dynamic recrystallization. The dynamic recrystallization is a recrystallization procedure that occurs at elevated temperature deformation, where the nucleation and expansion of new grains occur during the deformation process due to local temperature rise into the FSP zone [34]. As EBSD images reveal that at three passes the plastic flow of materials improves and severe deformation reduces the amount and size of agglomeration, leading to a better homogeneous distribution of Y_2O_3 (Fig. 3a), HA (Fig. 3b), and ZrO_2 (Fig. 3c) particles into the AZ91D matrix. But the AZ91D/Y_2O_3 surface matrix (Fig. 3d) shows a better refined average grain size (2.5 µm) as compared to AZ91D/HA (Fig. 3e) and AZ91D/ZrO_2 (Fig. 3f) matrix (such as 3.1 and 2.7 µm) because it may be connected to grain boundaries which hamper grain border relocation and subsequent grain growth due to the presence of ZrO_2 particles. Hence this is a significant factor in dynamic recrystallization and grain refinement phenomena.

The EDS counts analysis using the EBSD technique shows factors affecting the light-scattering properties of the polycrystalline materials, as shown in Fig. 4a–f. The grain size and grain boundary theses are the most affecting parameters to form a better microstructure in the FSPed zone. Furthermore, the Y_2O_3-reinforced surface (Fig. 4a and b) revealed better flow of material and refinement during FSP as compared to the HA- (Fig. 4c and d) and ZrO_2-reinforced surfaces (Fig. 4e and f). But, this may be due to the clustering of bigger metallic compounds that are formed. Also, it may occur due to the formation of a CSL boundary which is developed by the crystallographic orientation of the constituent crystal, as shown in Fig. 5a–i. The entire reinforcement particle was settled at the grain boundary during the flow of materials. The grains are not connected due to different crystallographic orientations [35]. Basically, the plane orientation at 3, 7, and 13b sigma-values is the same for the Y_2O_3-, HA-, and ZrO_2-reinforced composites, which show a lack of grain growth during the recrystallization process in FSP, as shown in Fig. 5c, f, and i. Hence, the crack initiation occurred for these reasons.

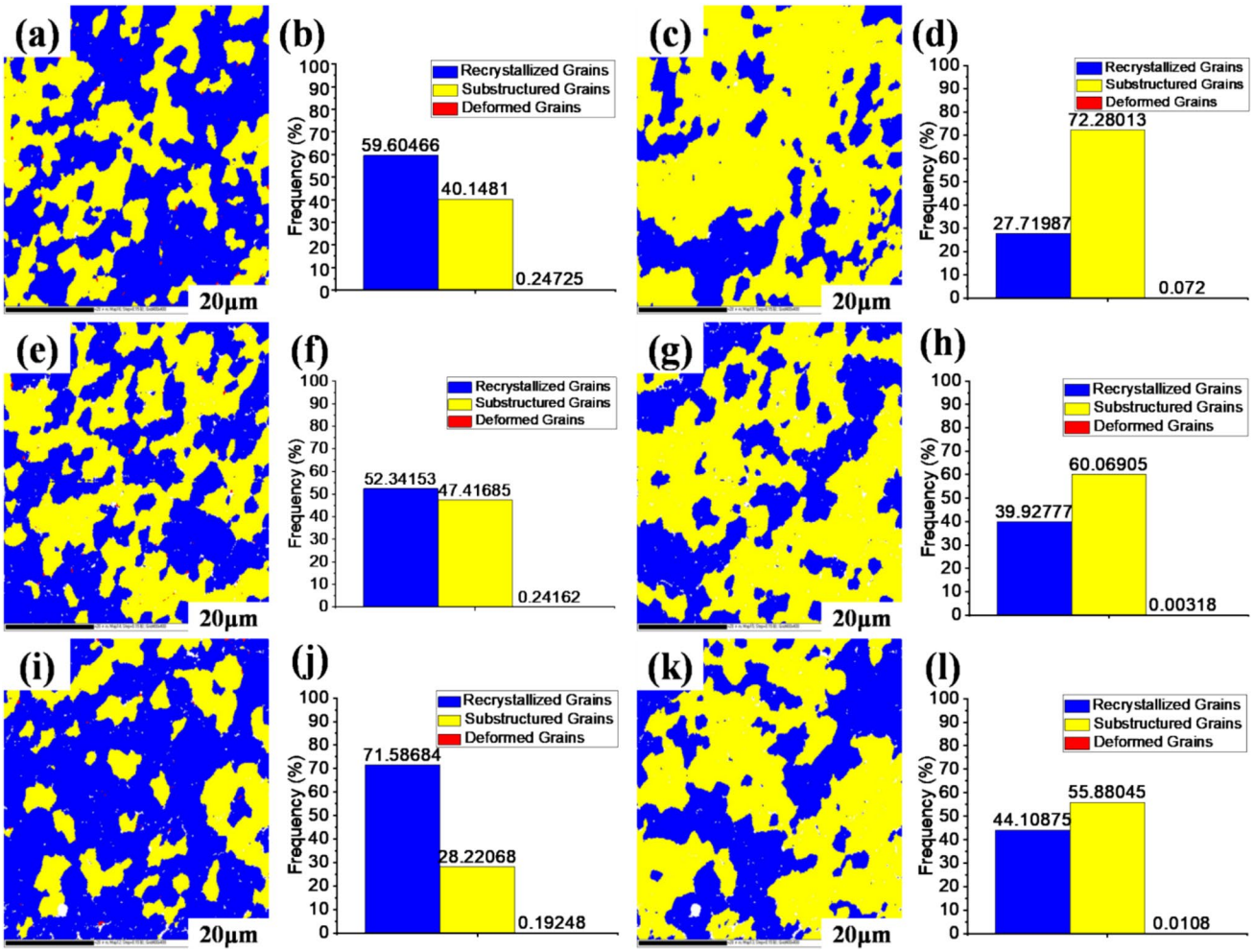

Fig. 7 Recrystallization fraction of the FSP surface composite at three passes. **a**–**d** AZ91D/Y_2O_3 composite at **a** and **b** 2° misorientation angle and **c** and **d** 15° misorientation angle; **e**–**h** AZ91D/HA composite at **e** and **f** 2° misorientation angle and **g** and **h** 15° misorientation angle; and **i**–**l** AZ91D/ZrO_2 composite at **i** and **j** 2° misorientation angle and **k** and **l** 15° misorientation angle

3.2 XRD evaluation

The XRD patterns of the AZ91D alloy and FSPed surface with incorporation of Y_2O_3, HA, and ZrO_2 particles after three passes are presented in Fig. 6. The peaks of the FSP surface are mainly comprised of α-Mg, $Mg_{93}Pb_7$, and $Mg_{0.97}Zn_{0.3}$, but the content of Mg-Zn compounds decreased significantly after increasing the homogeneity of the reinforcement particles in the surface matrix. These results indicated that FSP did not alter the phase composition of the Mg-Zn compounds. The Y_2O_3 peaks are higher than the ZrO_2 peaks because of the less texture and breakage during FSP. Hence, the ZrO_2 compounds are homogenous and available on the surface in the different plane positions. Furthermore, the HA-reinforced surface matrix shows two different CaO and PO_2 contents, which occur due to recitative behavior and dissolution of partial precipitates in anisotropy texture in the matrix.

For AZ91D alloy, the diffraction patterns of α-Mg contained a larger peak of (0002) plane rather than a lower peak of (0001) plane, including no evident preferred orientation. In the FSPed composite, the peak intensity of the (01–10) reduced significantly, but the peak intensity of (0002) was quite high. This indicates that the plane (0002) is transverse to the surface plane. The (0002) plane on the rolling or extrusion flat plane is frequent in hexagonal magnesium alloy. Therefore, the FSP tool moves over the plate under compressive stress, causing dislocation of the grains parallel to the process zone during FSP [36]. Similarly, increased passes induced preferential orientation and produced a shear deformation plane of (0002). But (0002) peak of FSPed composite is displaced and expanded compared to the AZ91D alloy matrix. Hence, it could be attributed to the presence of HA and ZrO_2 particles due to less grain movement. Also, the intensity of the (01–10), (01–12), and (11–20) for Y_2O_3-,

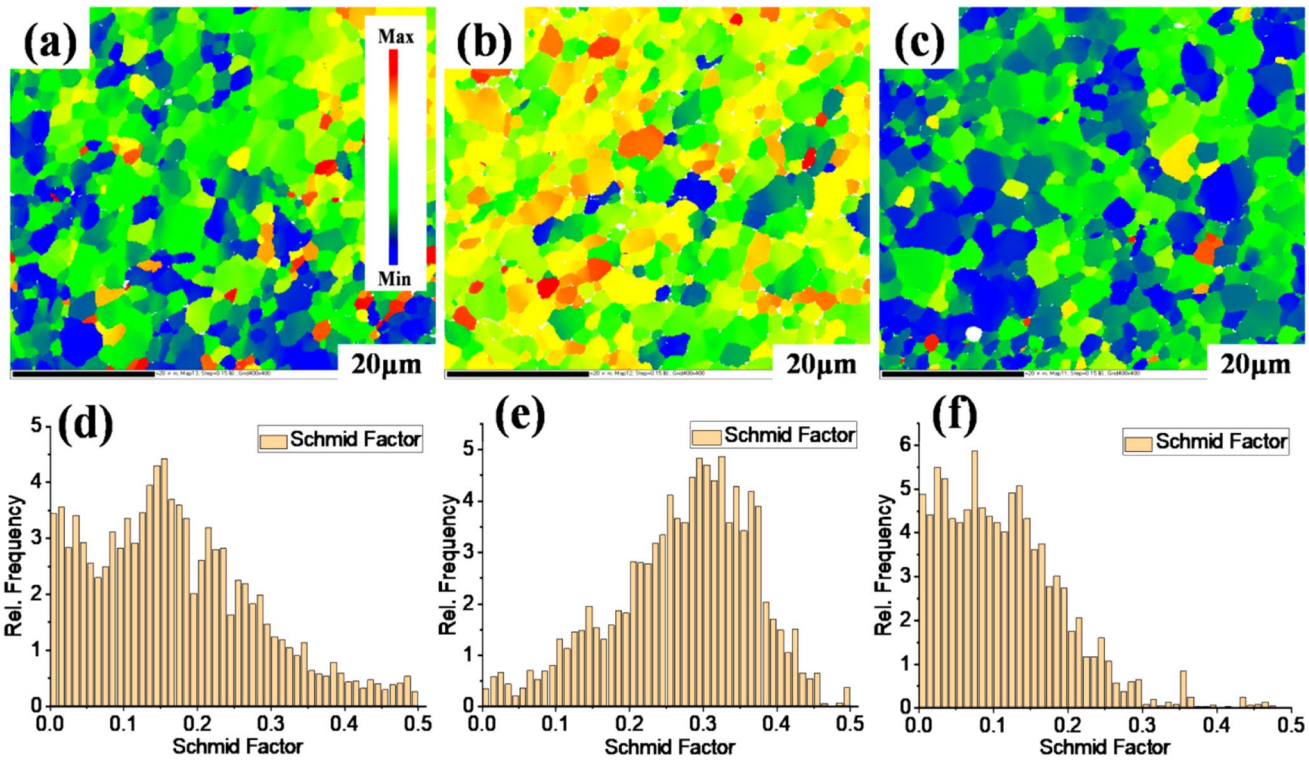

Fig. 8 Schmid factor of FSP surface composite at {0001} plane and <11–20> slip direction after three passes; **a** AZ91D/Y_2O_3 composite and its **d** corresponding plane orientations, **b** AZ91D/HA composite and its **e** corresponding plane orientations, and **c** AZ91D/ZrO_2 composite and its **f** corresponding plane orientations

HA-, and ZrO_2-reinforced surface diffraction peaks are small and stable, whereas the (211) peak changes significantly.

3.3 Texture evaluation

Figure 7a–l shows the recrystallization fraction of the FSP surface composite. The recrystallized grains are higher in ZrO_2-reinforced surface composite (Fig. 7i–l) as compared to the Y_2O_3- (Fig. 7a–d) and HA-reinforced (Fig. 7d–f) surfaces at 2° and 15° misorientation angles. Whereas the substructure grain is higher in the Y_2O_3-reinforced surface at 15° misorientation as compared to HA- and ZrO_2-reinforced surfaces. So this phenomenon may occur at higher grain circulation during FSP, and the grain size is much smaller in the deformed state in the FSP matrix and may also have higher heterogeneous grain arrangement in the recrystallized state, where very large grains and a lot of very small twins are presented simultaneously. However, in both cases, the recrystallized volume fractions may affect the estimated microhardness of the FSP sample.

Although the dislocation consists of several grains that must co-deform, each grain's dislocation is effectively a single crystal, and the flow stress of a single crystal is strongly dependent on the angle of the slip plane relative to the applied forces, a phenomenon characterized by the Schmid factor for single crystals and the Taylor factor for polycrystals, as shown in Fig. 8a–f. Figures 8b and e show that high crystal orientation may alter the tensile strength of AZ91D/ZrO_2FSP matrix surface, which contributes to enhancement in point defects and impurity migration as compared to the AZ91D/Y_2O_3 (Fig. 8a and d) and AZ91D/HA composite (Fig. 8c and f). The primary cause of dislocation generation is slip due to thermal stress during crystal growth. Thermoelastic stress is the result of a steep thermal gradient in the crystal growth system; typically, a high density of dislocations occurs due to pulled crystals [37].

As a result, an initial dislocation moves across the crystal lattice until the grain boundary blocks it. However, there are other grains besides the boundary that limit its dislocation, such as the grain's texture. And other dislocations such as cluster grains may act a similar texture behavior. Also shows the primary dislocation of two dislocations in separate planes. At a certain level of deformation, it may come together in the lattice area and form a dislocation junction [38]. The dislocation density clearly shows that the quantity of dislocation mainly affected the tensile strength and plastic deformation.

In view of the circulation of dislocations in a single slip plane, the displaced dislocations at various deviations tend to pile up in places where the movement of dislocations is

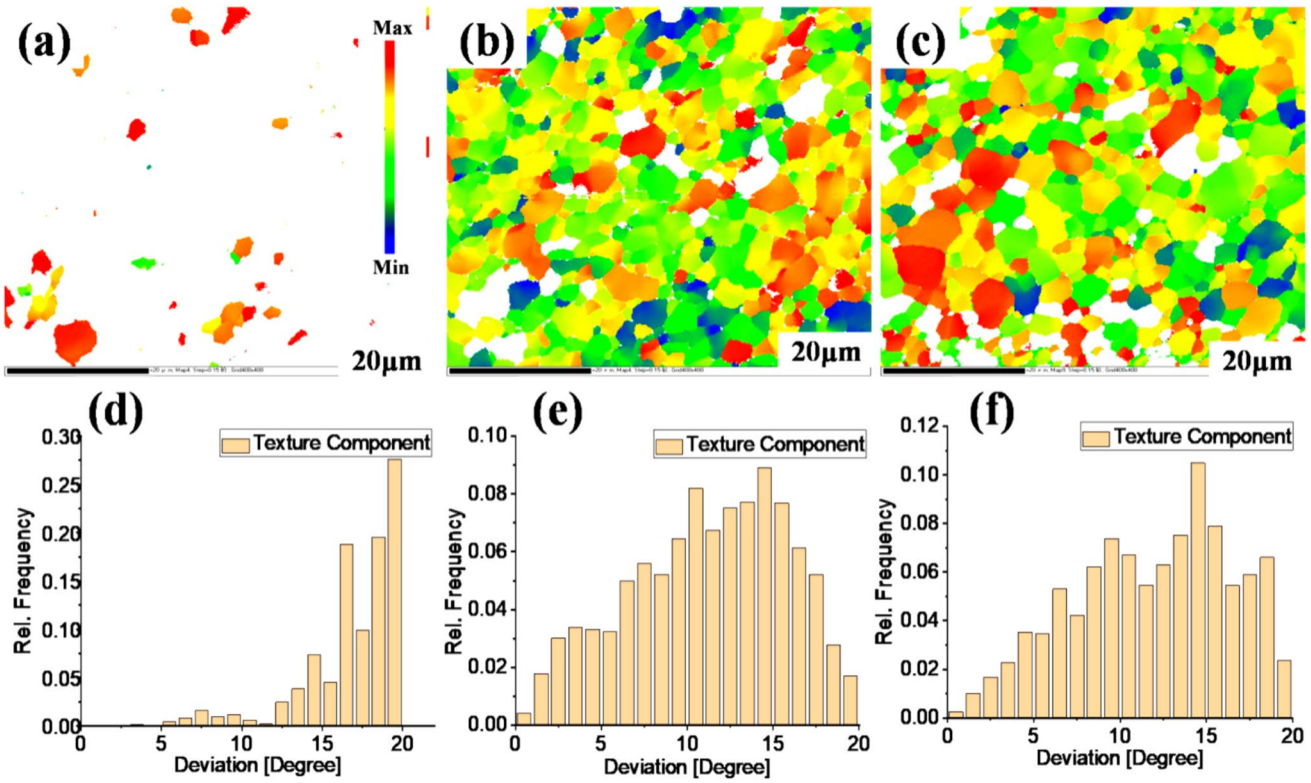

Fig. 9 Texture component of FSP surface composite at {0001} plane and < 11–20 > slip direction after three passes; **a** AZ91D/Y_2O_3 composite and its **d** corresponding plane orientations, **b** AZ91D/HA composite and its **e** corresponding plane orientations, and **c** AZ91D/ZrO_2 composite and its **f** corresponding plane orientations

restricted between grain boundaries, thus the texture grains are very low with the reinforcement of the Y_2O_3 particles (Fig. 9a and d) as compared to HA (Fig. 9b and e) and ZrO_2 particles (Fig. 9c and f). Thus, inter-atomic forces occur in the pileups which result in developed back stresses. The back stresses reduce grain sliding due to connecting the developed shear stresses between each of the grains so grain dislocation movement reduces. These phenomena are known as kinematic strain hardening [39]. Furthermore, the phenomenon causing stress gradients is complicated by the occurrence of different pileups which are also attributed to enhanced yield stress. Further, the kinds of developed precipitates are also attached to the dislocations and affect the grain hardening in the FSPed surface matrix.

Figures 10a–c, 11a–c, and 12a–c show {0001} pole figures, angles of pole tilting, and inverse pole figures of the Y_2O_3-, HA-, and ZrO_2-reinforced AD91D surface composite. The reinforced FSPed AZ91d surface shows a strong basal type texture in < 11–20 > slip direction. The majority of the grains are refined and aligned in the processing direction with a peak texture intensity of 67.99 for Y_2O_3 (Fig. 10a and b), 59.16 for HA (Fig. 11a and b), and 89.45 for ZrO_2 (Fig. 12a and b) reinforced surface composite. Correspondingly, the inverse pole figures show a high intensity at < 11–20 > direction parallel to the processing direction which is also known as < 11–20 > texture component. The peak texture intensity, as compared to the ZrO_2-reinforced surface, decreased by 21.46 and 30.29 for HA- and Y_2O_3-reinforced surfaces, respectively. The reduction in maximum texture intensity compared to the ZrO_2-reinforced surface occurs due to the clustering of the particles into the substrate matrix during the FSP. But the distinct feature is that the < 11–20 > texture component disappears at Y_2O_3- and ZrO_2-reinforced surfaces, while the HA-reinforced surface is seen near < 10–10 > texture component.

Moreover, Figs. 10c, 11c, and 12c show inverse pole figures of the FSPed surface composite, which reveal a more homogenous characteristic of Y_2O_3- and ZrO_2-reinforced surfaces, while the HA-reinforced surface shows a less homogeneity may including twins and shear bond. The slip direction < 11–20 > for the {0001} plane shows a related misorientation angle into the FSP surface matrix. Inside grain misorientation axes analysis, the identified slip modes throughout the misorientation angle range are 10–80°. The misorientation axis may be shown to be intense around < 11–20 > slip direction indicating the activation basal slip during deformation. Hence, the activation of basal slip formed a fully recrystallized grain structure which is responsible for the

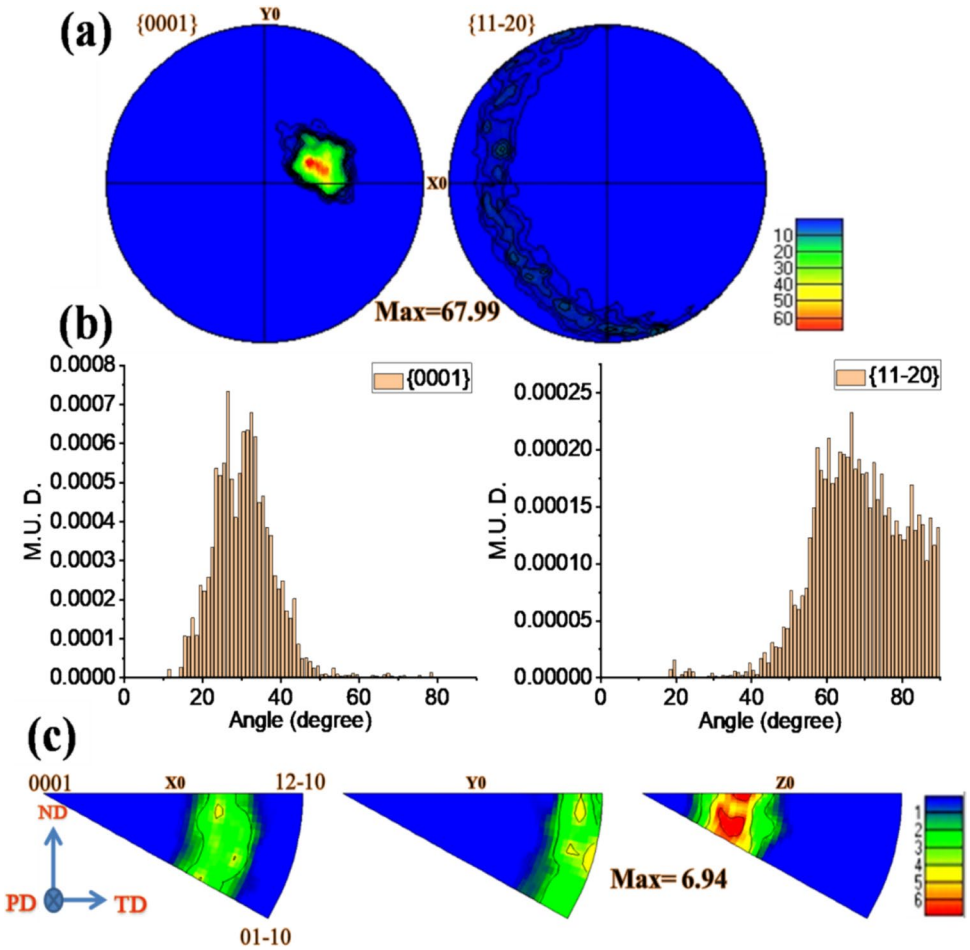

Fig. 10 **a** Pole figures of $AZ91D/Y_2O_3$ FSP surface composite at {0001} plane and < 11–20 > slip direction after three passes, **b** multi uniform distribution of the plane at different misorientation angles, and **c** inverse pole figures

higher grain growth and gradually increased average grain size in the matrix [40]. The mud is almost equal for the HA- and ZrO_2-reinforced surfaces, but for the Y_2O_3-reinforced surface, mud change of basal poles is in the range of 40–90°. In addition, from the viewpoint of the inverse pole figure, recrystallized grains belonging to the <01–10> texture component show better growth behavior. Corresponding to {0001} inverse pole figures, when all recrystallized grains are considered together, both <11–20> and <01–10> texture components as revealed in Figs. 10c, 11c, and 12c. By comparing the inverse pole figures in the processing direction corresponding to large and small recrystallized grain individually, it may be reduced that texture component, whereas large recrystallized grain are predominately correlated to <01–10> texture component. Therefore, the texture component <01–10> may enhance the grain strengthening due to the expanse of small recrystallized grains and their growth.

In addition, rotation axes of these grain boundaries with relatively high misorientation angles are 20–45°, 40–70°, and 35–70° for Y_2O_3-, HA-, and ZrO_2-reinforced surface matrices. The grain boundaries with the misorientation degree around ~40° (40–45°) [0001] are frequently shown in Mg-alloy, which is reported to relate to the coincident site lattice (CSL) of Σ13b. Hence, Σ13b has relatively low energy and leads to a depression in the continuous energy curve. Therefore, a close 40° boundary near Σ13b has perfect properties in structure and is more stable in energy, as shown in Fig. 5c, f, and i. Accordingly, grain boundaries at 45°, 55° <01–10>, and 77° <11–20> are identified as low-energy grain boundaries, which are readily reversed during grain growth. The increase in the frequency of these low-energy grain boundaries at the cost of high-energy boundaries is due to the reduction in the system energy [41]. Furthermore, recrystallized grains belonging to the < 11–20 > texture component show a misorientation of 40–45° [0001], which has a growth advantage from an energy perspective. Therefore, it is reasonable to attribute the enhancement of the < 11–20 > texture component to the preferential growth of recrystallization grains with low-energy grain boundaries.

The intensity distributions of the FSP composite were observed at Φ-angles and $\varphi 1$-angles for a single basal slip component. The processed composite creates better intensity on the basal slip component at (Φ) 90° and ($\phi 1$) 180° and ($\Phi 2$) 0°, 30°, and 60°. The ODF functions (Fig. 13a–f) and GDF (Fig. 14a–f) of FSP composites showed basal plane

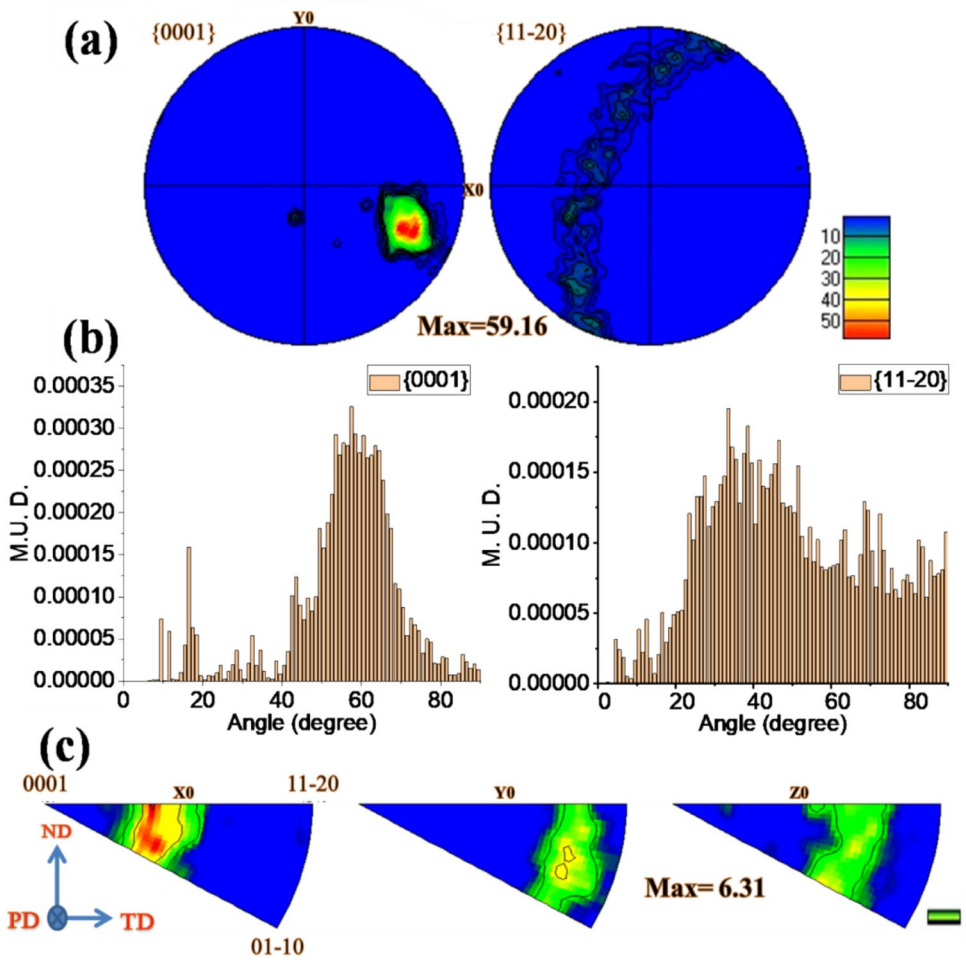

Fig. 11 **a** Pole figures of AZ91D/HA FSP surface composite at {0001} plane and < 11–20 > slip direction after three passes, **b** multi uniform distribution of the plane at different misorientation angles, and **c** inverse pole figures

dislocation at the Φ_2-angle between 30° and 60°. However, their main texture shows limited basal texture of {0001} < 11–20 > plane; the more reductions weakened the initial texture, resulting in lower intensities than the substrate material. Also, the more intensity distributions at φ_1-angles may reduce the strength of the basal texture, especially at $\varphi_1 =$ 30°. Therefore, the texture of the FSP composite resulted in ({0001} < 11–20 > and {0001} < 01–10 > types of crystallographic orientation due to dynamic recrystallization and deformation mechanisms. Thus, the non-basal slips, such as pyramidal slips and prismatic slips, activated, which significantly weakened the primary basal texture and generated more texture components along the FSP direction [42]. Hence, as per conclusions, the Y_2O_3-reinforced surface matrix has a higher basal texture as compared to HA- and ZrO_2-reinforced surface matrices during FSP, which is responsible for higher grain refinement into the matrix.

3.4 Microhardness evaluation

Figure 15a–c shows the histogram of the microhardness value ofAZ91D alloy andY_2O_3-, HA-, and ZrO_2-reinforced FSPed AZ91D alloy surface composite in the stirring zone after multi passes. Consequently, it was found that the distribution of reinforced particles and grain refinements are the primary causes of the increased instability of the microhardness value for FSPed composite compared to substrate alloy. The number of FSP passes affects not only the dispersion of particles but also the grains dislocation. After the first and second pass, the reinforced composite had significant fluctuations in microhardness in the FSP zone because the reinforcement particles were less homogeneously distributed. However, the microhardness of the reinforced FSPed AZ91D surface composite reveals rather steady fluctuation values at three passes. This suggests that the reinforcement particles are distributed more uniformly throughout the AZ91D matrix, which is more consistent with improved microstructural behavior. With an increased pass, the AZ91D/ZrO_2 composites show improved microhardness (Fig. 15c), compared to the AZ91D/Y_2O_3 composite (Fig. 15a) and AZ91D/HA composite (Fig. 15b) due to better grain size reduction. Therefore, strengthening the grain boundary was the most important reason for the increase in microhardness. The heterogeneous nucleation of $Mg_{93}Pb_7$ and $Mg_{0.97}Zn_{0.3}$

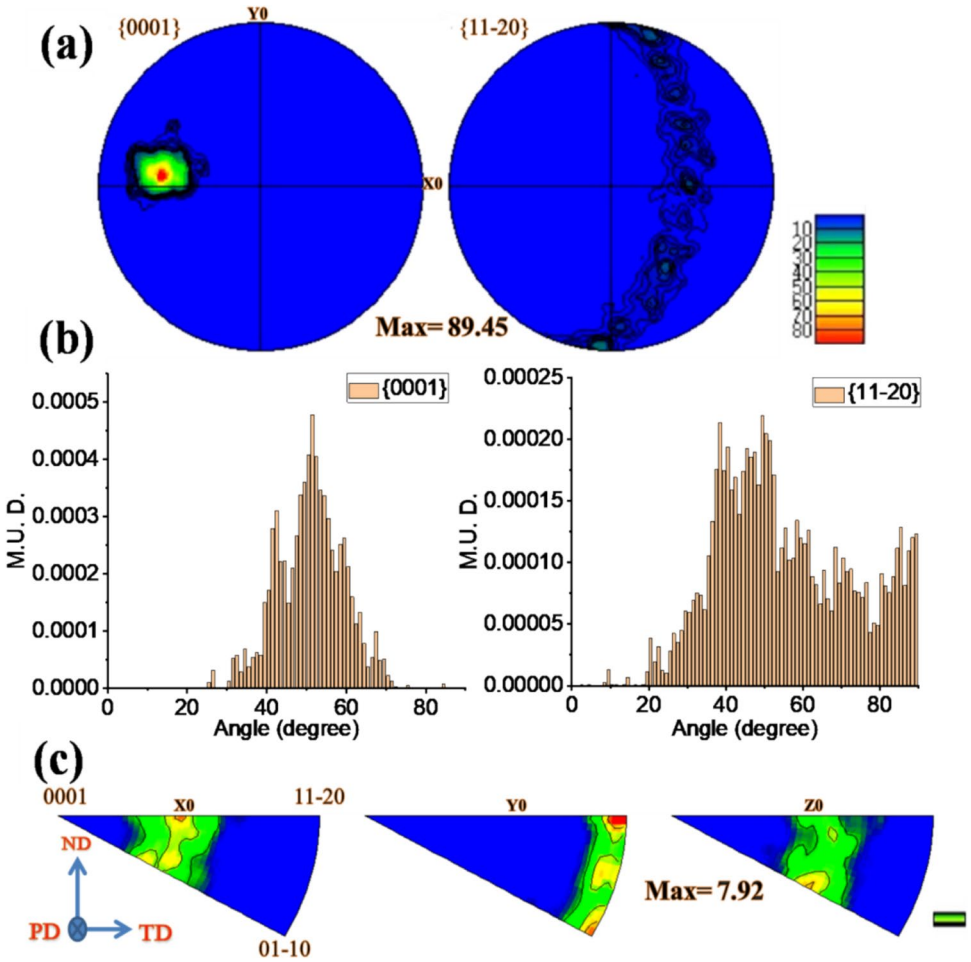

Fig. 12 **a** Pole figures of $AZ91D/ZrO_2$ FSP surface composite at {0001} plane and <11–20> slip direction after three passes **b** multi uniform distribution of the plane at different misorientation angles, and **c** inverse pole figures

effectively reduced the dislocation movement and grain boundary sliding, which play a vital role in better reinforcement distribution during FSP and increased microstructure homogeneity. As a result, tiny fragments of the intermetallic phase α-Mg, $Mg_{93}Pb_7$, and $Mg_{0.97}Zn_{0.3}$ are consistently dispersed throughout α-Mg. Hence, the reinforced FSP composite had enhanced microhardness compared to the base AZ91D alloy.

3.5 Tensile property

The uniaxial tensile tests of the AZ91D alloy and FSPed samples were performed to examine the effect of the reinforcement incorporation after different FSPed passes, as shown in Fig. 16a–f. The modified stress and strain curves were observed after one, two, and three passes with incorporation of the Y_2O_3- (Fig. 16a), HA- (Fig. 16c), and ZrO_2- (Fig. 16e) reinforced AZ91D surface composite. It was obvious that the monolithic feature of the reinforced AZ91D alloy composite had an inhomogeneous microstructure that exhibited slightly enhanced UTS (159.1 MPa) for $AZ91D/ZrO_2$ (Fig. 16f) compared to (132.2 MPa) of the AZ91D/HA (Fig. 16d) and (157.6 MPa) of the $AZ91D/Y_2O_3$ (Fig. 16f) surface composite. Meanwhile, after FSP, the tensile strength decreased significantly for the AZ91D alloy. The tensile strength of FSP composites was decreased due to better flow of reinforcement particles toward the grain boundary and improper distribution into the FSP matrix. In addition, the strengthening mechanisms for the AZ91D alloy metal matrix composites are mainly direct and indirect strengthening. Since the tensile strength of FSP composite particles was low, they could not directly bear the transferred load from the magnesium matrix to the reinforcement through the interface.

To acclimatize the decreased applied strain throughout the tensile test, basic deformation types take place due to lower critical resolved shear stress (CRSS) including the reduced tension twinning as well as active basal slip [43]. Hence, strain localization occurs which develops an arranged crystallographic structure for basal slip into the FSPed zone [44]. Thus, strain localization contributes to reduced tensile strength of the FSPed AZ91D alloy than

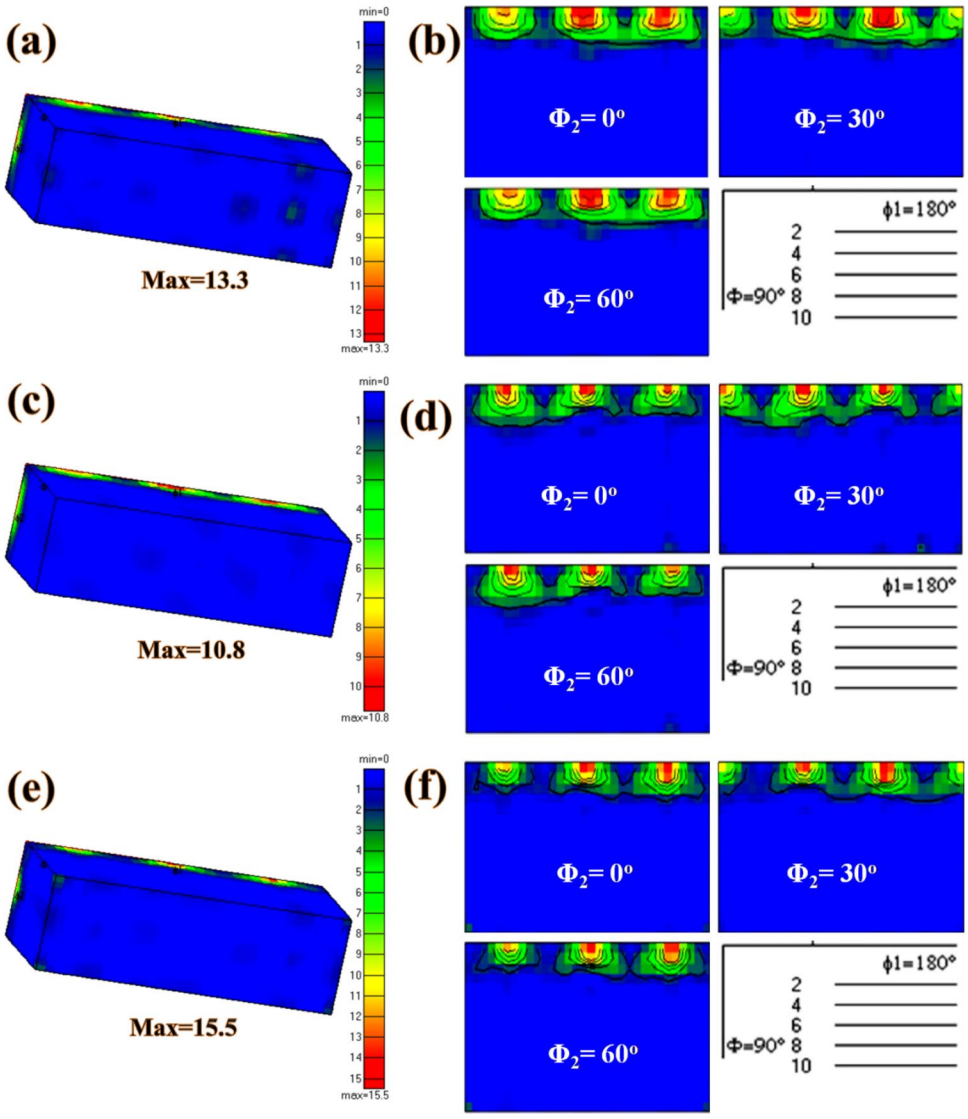

Fig. 13 ODF of FSP surface composite after three passes. **a** Grain distribution function of AZ91D/Y_2O_3 composite and **b** texture serial section at 0°, 30°, and 60°; **c** grain distribution function of AZ91D/HA composite and d texture serial section at 0°, 30°, and 60°; and **e** grain distribution function of AZ91D/ZrO_2 composite and **f** texture serial section at 0°, 30°, and 60°

the base AZ91D alloy. Furthermore, the clusters were decreased with increasing the passes, which was responsible for higher grain refinement into the matrix and enhanced the ultimate tensile strength after crossing the yield load.

Furthermore, a slight enhancement in ultimate tensile strength and a slight decrease in percentage in the elongation of the FSPed composite were observed with increasing grain refinement [45]. Also, the dispersion of reinforcement particles provided sufficient resistance to increasing the tensile strength. Moreover, the refinement of the reinforcement-based clusters may lead to an enhancement in ductility, resulting in the enhancement of the tensile strength of the fabricated surface composites at three passes. The evenly dispersed reinforced particles may enhance material flow and decrease early breakage, leading to an increase in the FSP composite's elongation. However, grain size was drastically reduced during the FSP process, which led to more uniform plastic deformation and an increase in ductility [46]. These strengthening mechanisms also examine Schmid's factor and Taylor's factor on grain strength, as shown in Figs. 8a–f and 17a–f.

3.6 Tensile fracture evaluation

The SEM image of tensile fracture surface analysis with EDS and elemental mapping of the AZ91D alloy (Fig. 18a–c) and AZ91D/Y_2O_3, AZ91D/HA, and AZ91D/ZrO_2 composites were shown after one, two, and three passes, as shown in Figs. 19, 20, and 21. Figure 19a–c for AZ91D/Y_2O_3, Fig. 20a–c for AZ91D/HA, and Fig. 21a–c for AZ91D/ZrO_2 show the fracture features after one pass. Similarly, Fig. 19d–f for AZ91D/Y_2O_3, Fig. 20d–f for AZ91D/HA, and Fig. 21d–f for AZ91D/ZrO_2 show the fracture features after two passes, and Fig. 19g–i for AZ91D/Y_2O_3, Fig. 20g–i for AZ91D/HA, and Fig. 21g–i for AZ91D/ZrO_2 show the

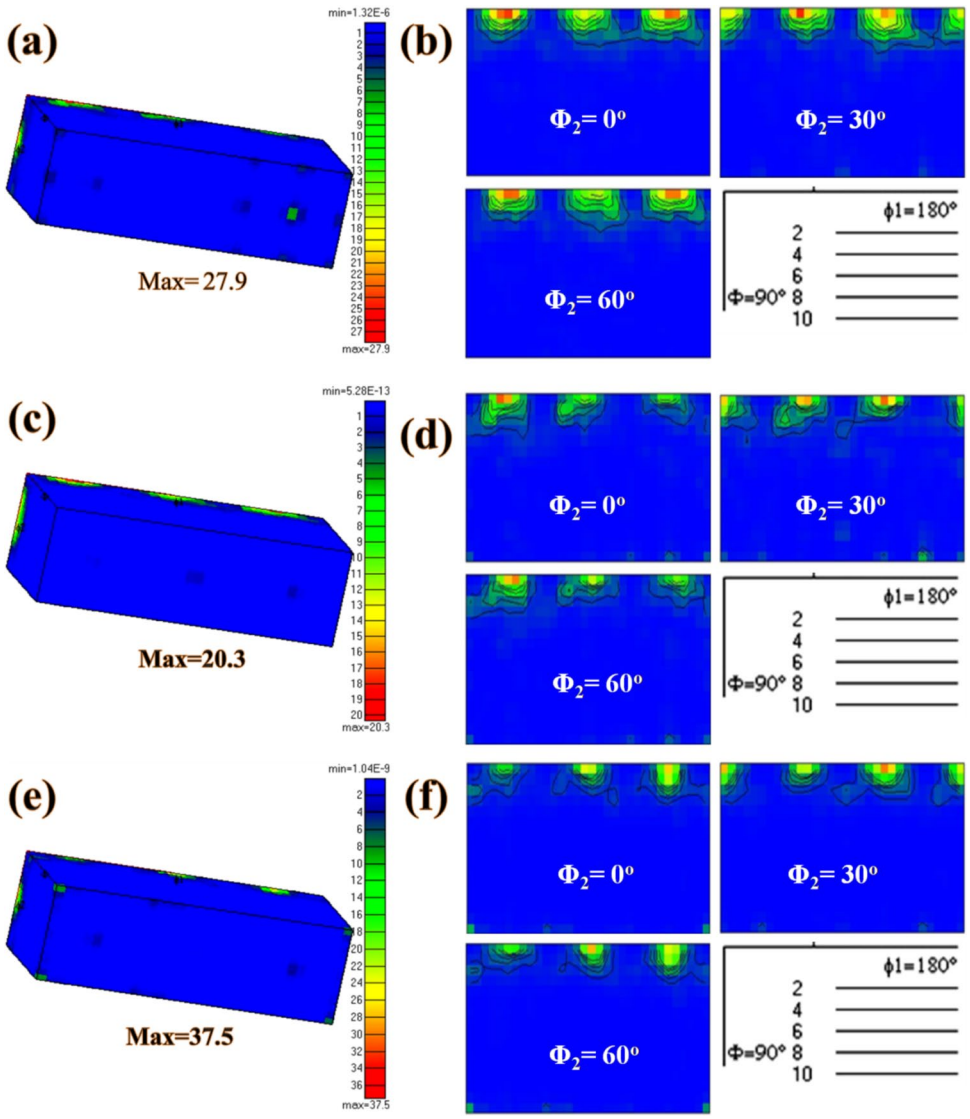

Fig. 14 Gaussian distribution function (GDF) of FSP surface composite after three passes. **a** Grain estimation of AZ91D/Y_2O_3 composite and **b** texture serial section at 0°, 30° and 60°; **c** grain estimation of AZ91D/HA composite and **d** texture serial section at 0°, 30° and 60°; and **e** grain estimation of AZ91D/ZrO_2 composite and **f** texture serial section at 0°, 30° and 60°

fracture features after three passes. The SEM image of fracture AZ91D alloy (Fig. 18a) shows a high number density of intense dimples as well as better wt% of Mg contents in EDS and elemental mapping (Fig. 18 (b and c)), which specifies the regular ductile manner of fracture. The increased dimples are also seen in FSPed samples with increasing FSP passes, which show that the fracture is more ductile for better dispersion of reinforcement particles (Fig. 19a, d, and g; Fig. 20a, d, and g; and Fig. 21a, d, and g).

The one-pass and two-pass samples fail hurriedly because the clusters of reinforcement particles splinter before the dimples completely form. Hence, mechanically mixed, brittle (Fig. 19a and d), and tiny dimple (Fig. 19g) types of fracture features and very diverse alloying elements are seen after one pass (Fig. 19b, c, e, f, h, and i)). Similarly, with reduced reinforcement clusters after two passes, the plastic deformed (Fig. 20a) micro crack, secondary cracks, quasi-cleavage (Fig. 20d) and layered types of fracture (Fig. 20g) seen, which may enhance the tensile strength of the composite as well as better formation of alloying elements (Fig. 20b, c, e, f, h, and i). Furthermore, after three passes, the uniform dispersion of incorporated particles resulted in the formation of well-shaped dimples with almost equal EDS alloying elements, as shown in Fig. 21b, c, e, f, h, and i. Meanwhile, the deep dimples (Fig. 21a) and honeycomb dimples (Fig. 21d) fracture features were increased, and micro-cracks cleavage planes and tear edge (Fig. 21g) fracture features were reduced. A significant proportion of dimples showed a ductile type of fracture due to a strong interfacial bond between the reinforcement particle and the Mg matrix.

To examine the strengthening impacts of the reinforcement particle on the fracture behavior that were observed after the tensile test. Compared to the HA and Y_2O_3-reinforced AZ91D surface composite, the ZrO_2-reinforced surface composite has a considerably

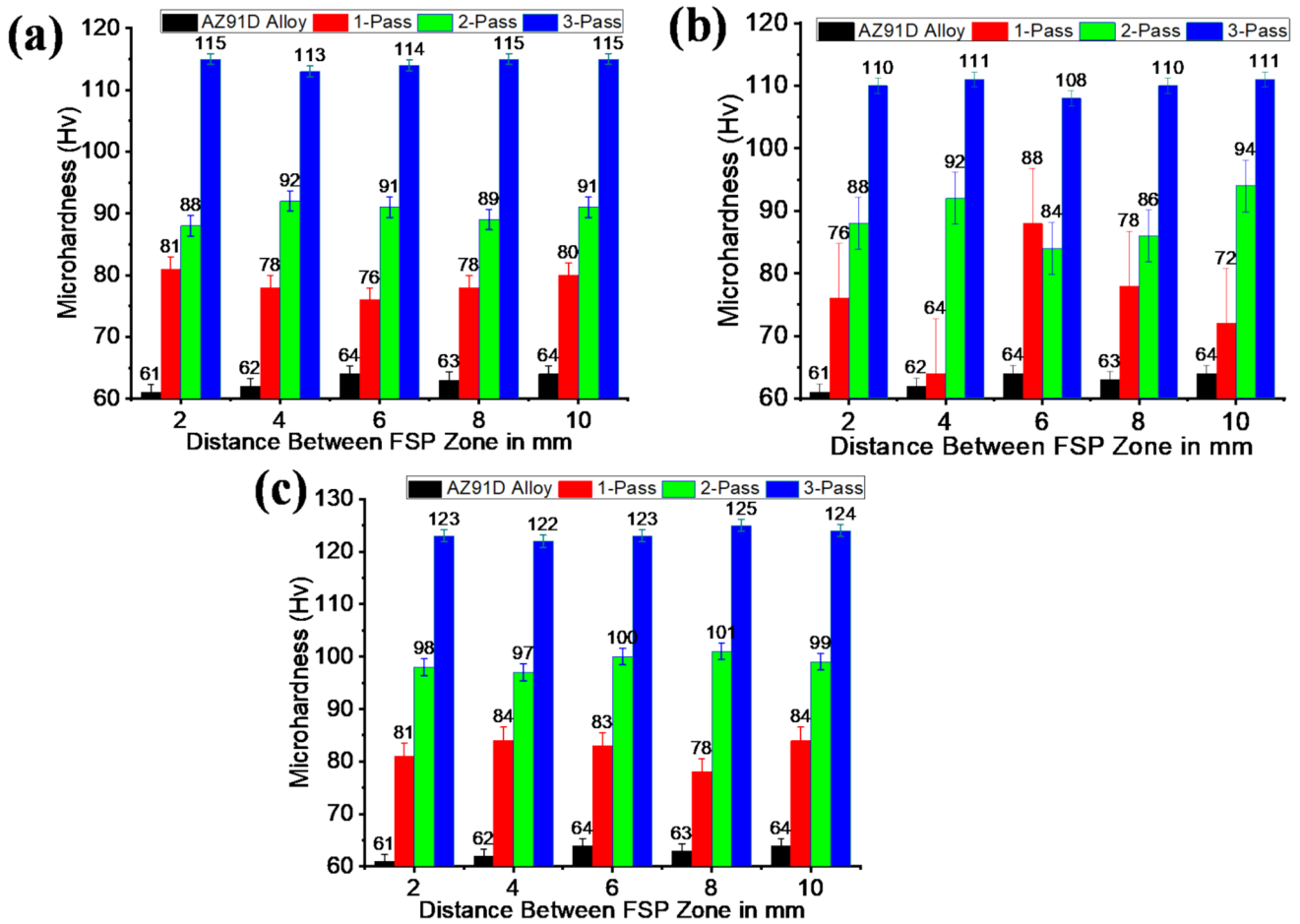

Fig. 15 Microhardness value of the AZ91D alloy and FSP surface composite. **a** AZ91D/Y_2O_3 surface composite, **b** AZ91D/HA surface composite, and **c** AZ91D/ZrO_2 surface composite

higher diffusion boundary, which is inhibited by the formation of HGBs as the main strengthening mechanism. Apart from the transgranular fracture, a few little dimples also started to grow, as shown in Fig. 3c and f. Hence, the fracture behavior changed to be more brittle and ductile in combination. Therefore, the increased number of passes was improving the dispersion of ZrO_2 particles, causing some grains to distort due to dislocation movement, which increased the dimples from one to three passes. Due to the increased dimples and extremely slow deformation during the tensile test, the fracture surfaces were formed by deep dimples, which are responsible for enhancing fracture strength.

3.7 Corrosion test evaluation

Figure 22a–c shows the loss of weight after 7, 15, and 30 days for the substrate alloy and reinforced FSPed samples. The substrate alloy shows more weight loss compared to reinforced FSPed AZ91D alloy, which is developed by FSPed surface composites. Figure 22a shows the gradually decreased weight loss for Y2O3-reinforced surface composite with increasing FSP passes and immersion days. As the FSP passes increased from one to three and immersion days from 7 to 30, the weight loss for FSPed samples gradually decreased for Y_2O_3-reinforced surface composites, as shown in Fig. 22a. But HA- and ZrO_2-reinforced FSP surface composite showed slightly higher weight loss with increased passes and immersion for 30 days, as shown in Fig. 22b and c. For 15 days of immersion, weight loss decreased compared with the 7 days of immersion. The dense chemical cluster effects exhibit that the incorporation of reinforcement enhances the corrosion resistance of the AZ91D alloy, which preserves that the corrosion resistance has enhanced due to better bio-mineralization with the addition of reinforcement particles. The corrosion rates of 30 days immersion for FSPed AZ91D/Y_2O_3 at one pass, AZ91D/Y_2O_3 at two passes, and AZ91D/Y_2O_3 at three passes were lower than the AZ91D alloy; the decreased weight loss was as 0.072 g, 0.052 g, 0.038 g, and 0.32

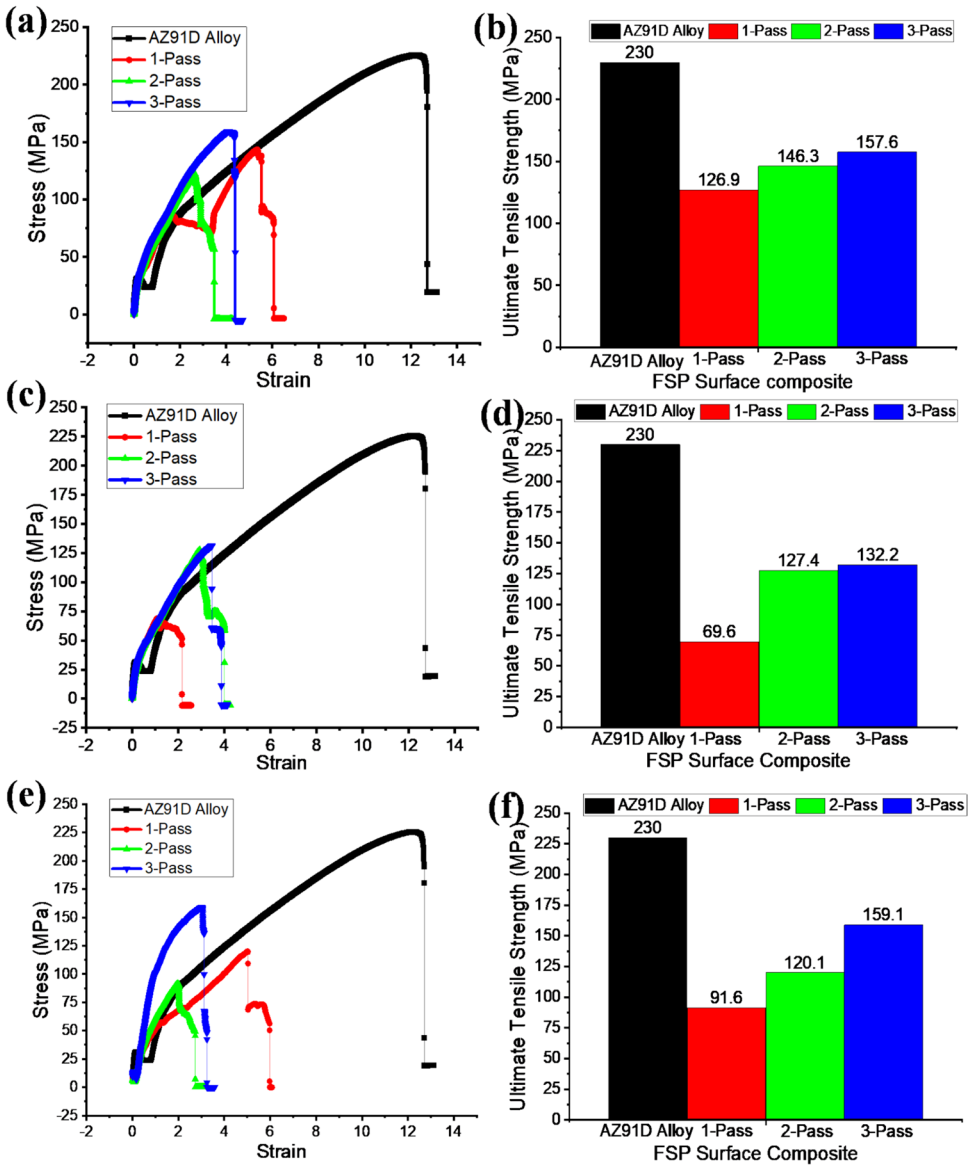

Fig. 16 Tensile strength of the AZ91D alloy and FSP surface composite. **a** AZ91D/Y_2O_3 surface composite and its **b** corresponding UTS value, **c** AZ91D/HA surface composite and its **d** corresponding UTS value, and **e** AZ91D/ZrO_2 surface composite and its **f** corresponding UTS value

g. Because the apatite layers and the comparatively more stable $Mg(OH)_2$ layer may have formed on the surface throughout the immersion phase, there was less weight loss. In an SBF solution, these generated layers are usually less soluble, protecting the immersion surface [47]. In the meantime, the deterioration rate improved as the number of FSP passes increased. Therefore, better uniform dispersion of Y_2O_3 nanoparticles may prevent localized corrosion with increased FSP passes. Furthermore, the HA and ZrO_2 reinforced surface composite had some lower corrosion resistance because they formed passive layers such as Ca/P and formed Zr-based oxide, which offers lower weight loss due to less reactive behavior in SBF solution [48]. Thus, the increased number of immersion days of composites shows reduced corrosion resistance.

3.7.1 Worn surface morphologies

Figures 23a–d, 24a–d, and Fig. 25a–d show the worn surface morphologies of the AZ91D alloy and AZ91D/Y_2O_3, AZ91D/HA, and AZ91D/ZrO_2 FSPed surface composite after three passes and after 7, 15, and 30 days of immersion corrosion tests. The typically corroded behavior is revealed on the surface of both the substrate metal and the fabricated samples. The substrate surface had higher deep pits and pitting corrosion as compared to the reinforced surface composite. It may occur due to the ionization generation of hydrogen produced during immersion days [49]. Also, the deep crack and crevice corrosion were observed due to the dehydration behavior of the FSPed surface, as shown in Figs. 23a, 24a, and 25a. In the FSP samples after 7 days of

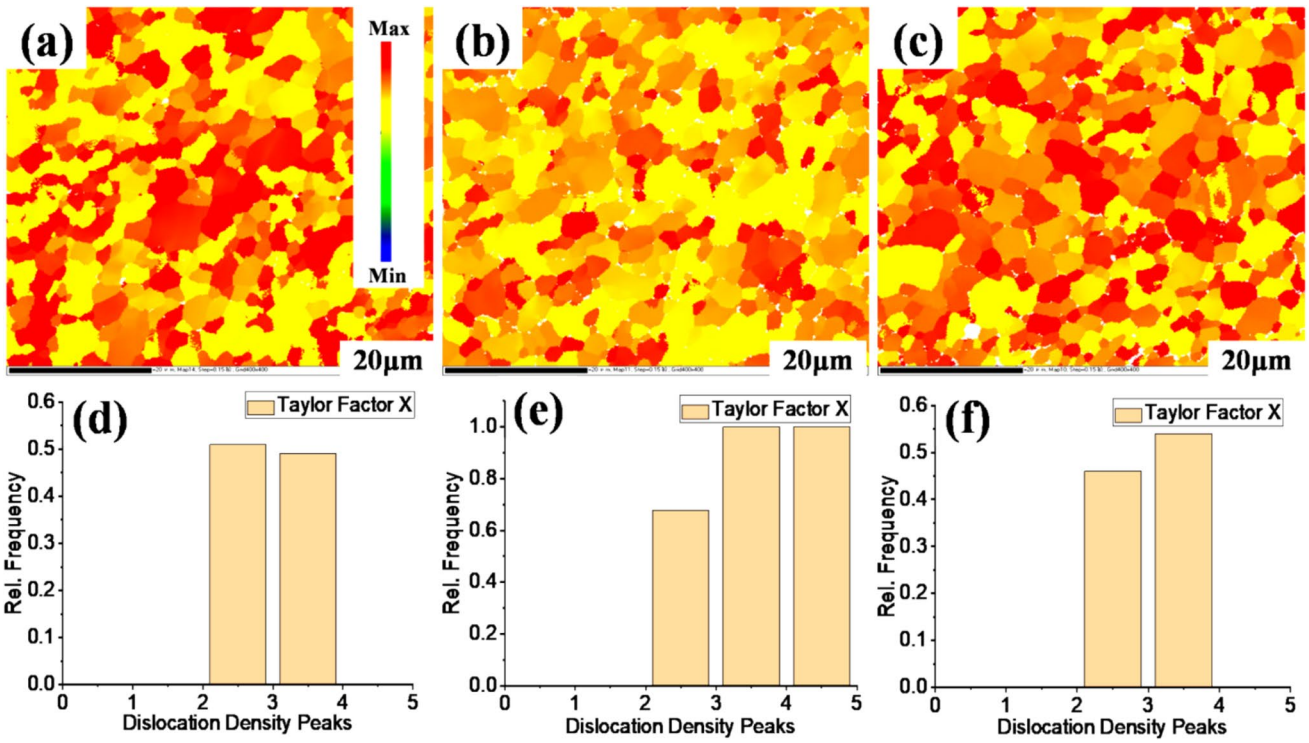

Fig. 17 Taylor factor of FSP surface composite at {0001} plane and < 11–20 > slip direction after three passes. **a** AZ91D/Y_2O_3 composite and its **d** corresponding plane orientations, **b** AZ91D/HA composite and its **e** corresponding plane orientations, and **c** AZ91D/ZrO_2 composite and its **f** corresponding plane orientations

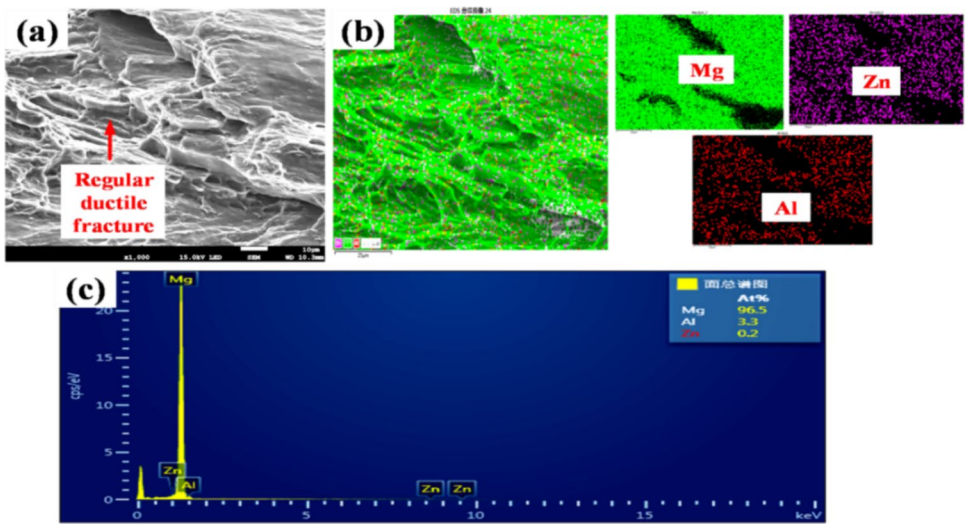

Fig. 18 Tensile fractured analysis AZ91D alloy. **a** SEM image of fractured AZ91D alloy, **b** elemental mapping, and **c** EDS image

immersion, the cracked types of corrosion occurred due to the released stress as well as increased bioactivity between the surface and the SBF solution [50], but as the Y_2O_3 reinforcement homogeneity increased in the surface matrix with increased passes, the corrosion occurred in a smooth layered manner with uniform pitting after 30 days of immersion as shown in Fig. 23d. Additionally, microbial corrosion was seen due to the formation of a weak passive layer on the surface. Hence, the increased passive layers enhanced the corrosion resistance with increasing immersion days.

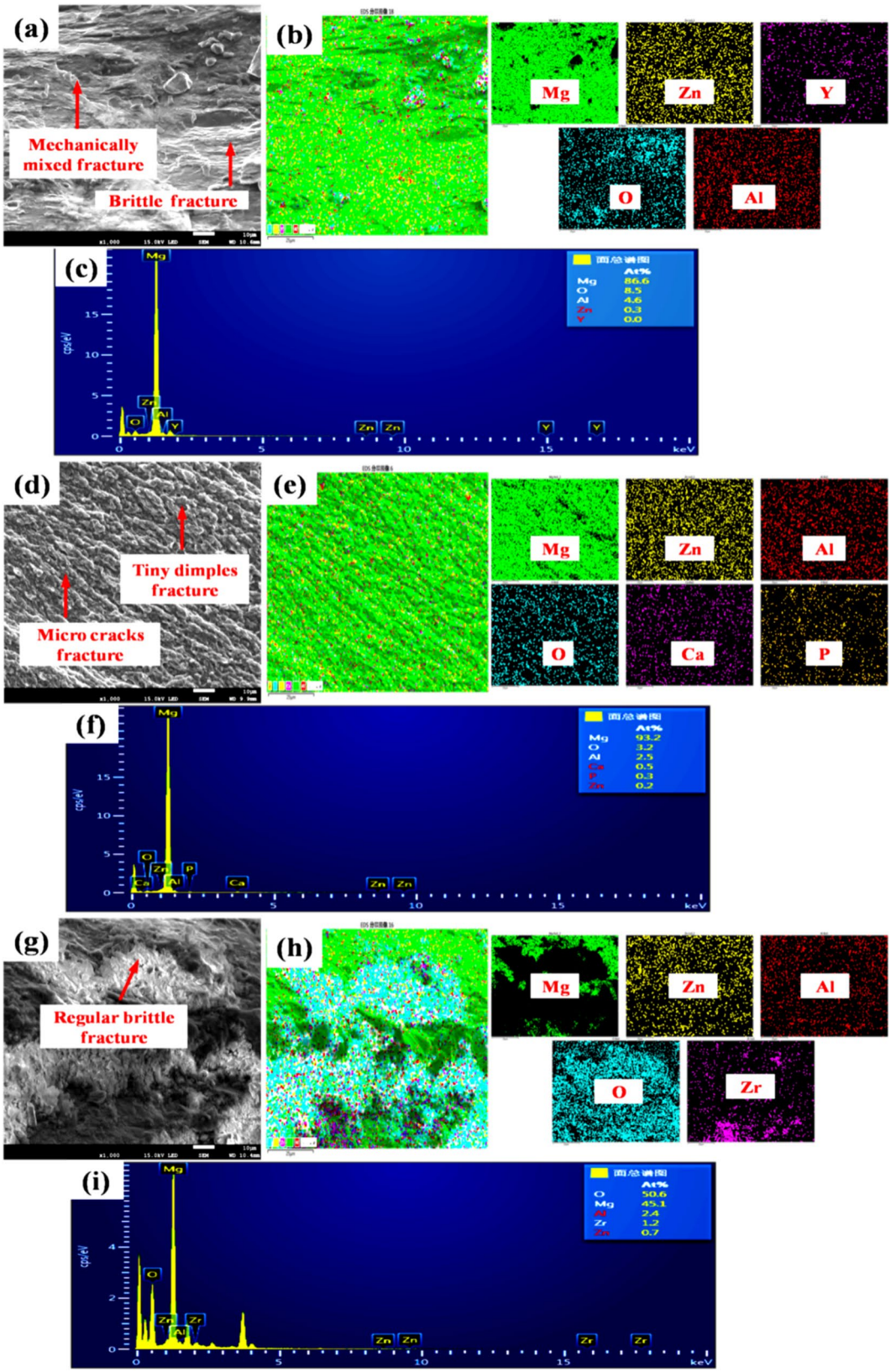

Fig. 19 Tensile fractured analysis after one pass, **a** SEM image of AZ91D/Y_2O_3 surface composite and **b** and **c** its corresponding elemental mapping and EDS image of the fractured surface, **d** SEM image of AZ91D/HA surface composite and **e** and **f** its corresponding elemental mapping and EDS image and **g** SEM image of AZ91D/ZrO_2 surface composite and **h** and **i** its corresponding elemental mapping and EDS image

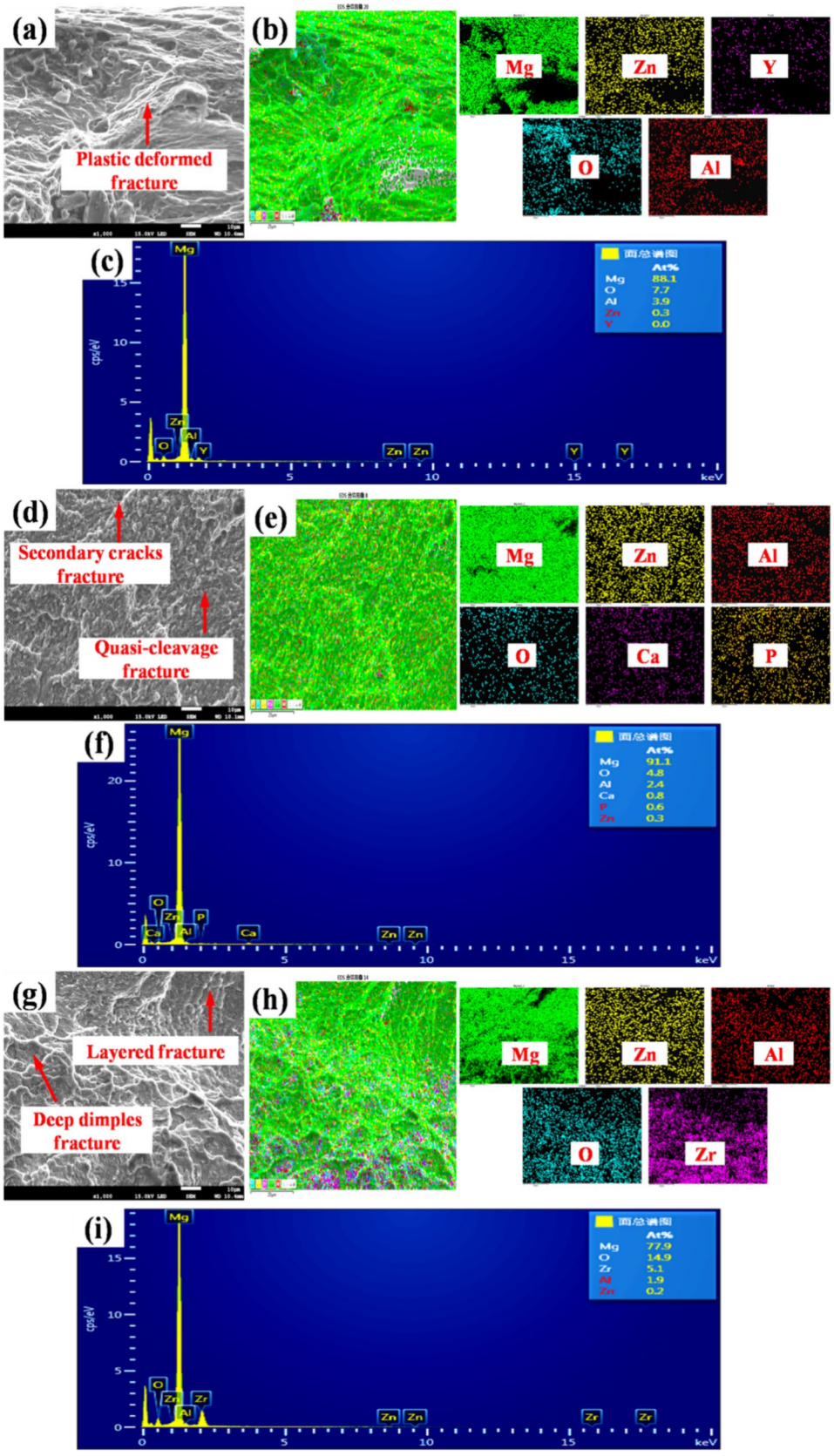

Fig. 20 Tensile fractured analysis after two pass. **a** SEM image of AZ91D/Y_2O_3 surface composite and **b** and **c** its corresponding elemental mapping and EDS image of the fractured surface, **d** SEM image of AZ91D/HA surface composite and **e** and **f** its corresponding elemental mapping and EDS image, and **g** SEM image of AZ91D/ZrO_2 surface composite and **h** and **i** corresponding elemental mapping and EDS image

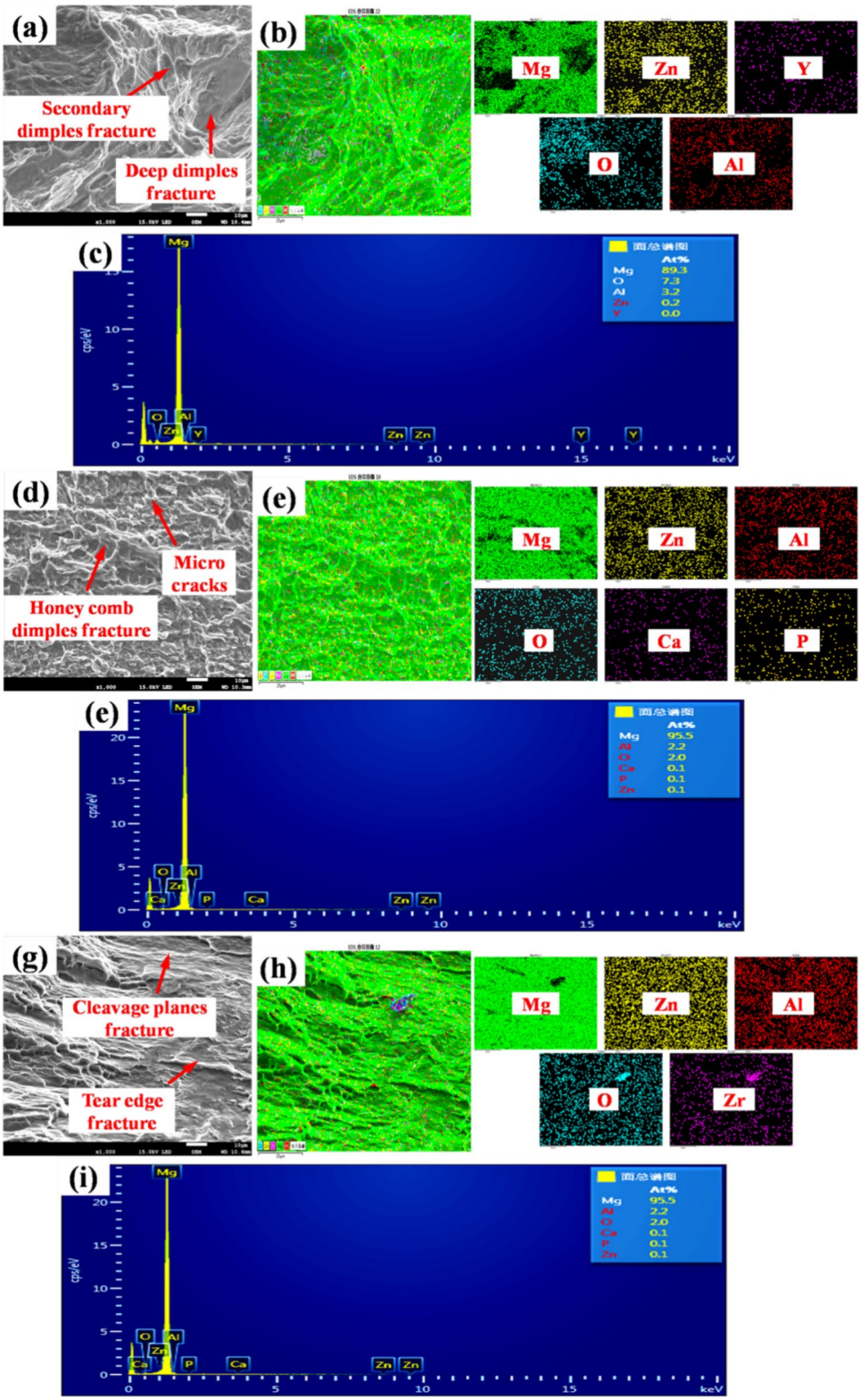

Fig. 21 Tensile fractured analysis after three passes. **a** SEM image of AZ91D/Y_2O_3 surface composite and **b** and **c** its corresponding elemental mapping and EDS image of the fractured surface, **d** SEM image of AZ91D/HA surface composite and **e** and **f** its corresponding elemental mapping and EDS image, and **g** SEM image of AZ91D/ZrO_2 surface composite and **h** and **i** its corresponding elemental mapping and EDS image

Furthermore, the HA-reinforced surface composite has relatively lower pitting and pits after 15 days of immersion, because the micro-cracked and Filiform structure for the surface was relatively more flat and uniform, while a large number of precipitates swelled and showed singular layers at the surface, as shown in Fig. 24c. According to studies, the primary corrosion behavior of the AZ91D alloy was affected due to containing calcium phosphate

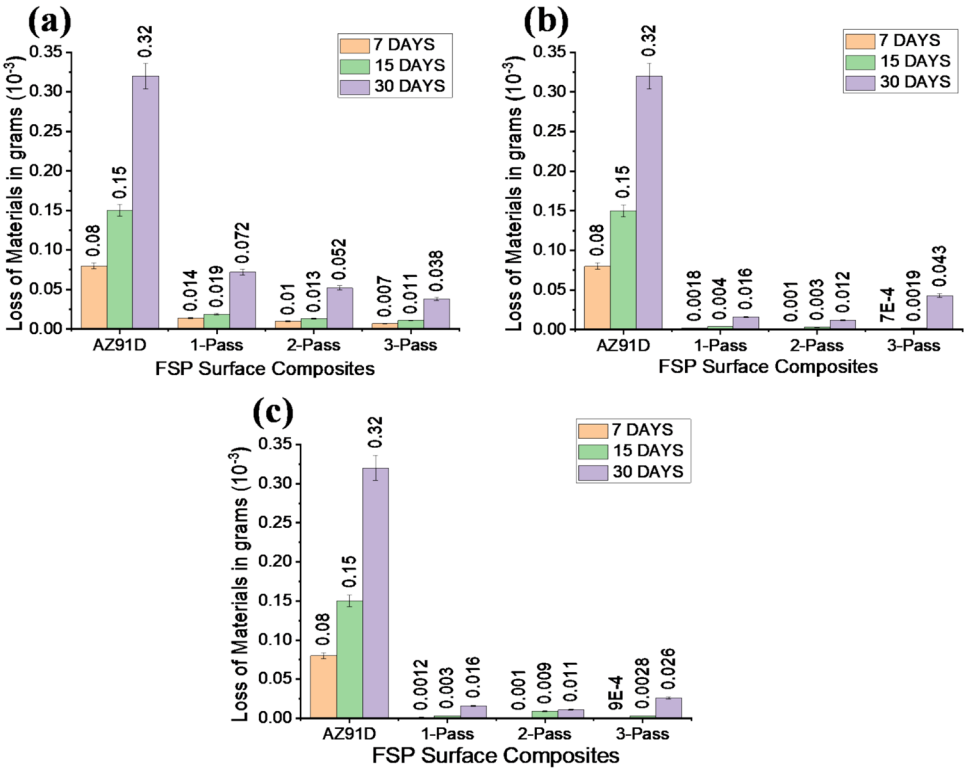

Fig. 22 Corrosion test result of the AZ91D alloy and FSP surface composite after one, two, and three passes at 7, 15, and 30 days immersion. **a** AZ91D/Y_2O_3 surface composite, **b** AZ91D/HA surface composite, and **c** AZ91D/ZrO_2 surface composite

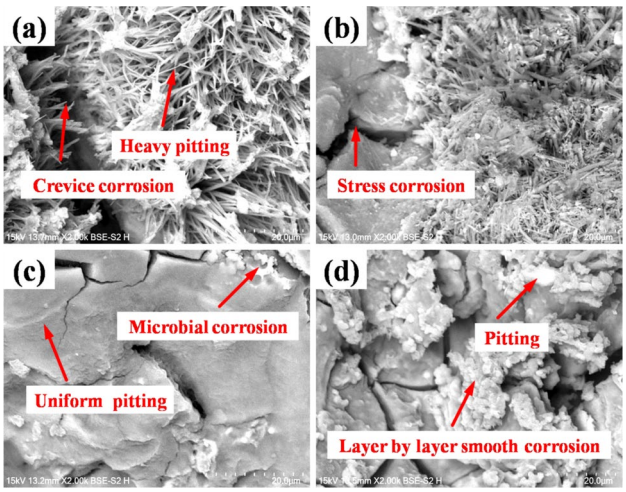

Fig. 23 Worn analysis after 7 days immersion. **a** AZ91D alloy, **b** AZ91D/Y_2O_3, **c** AZ91D/HA, and **d** AZ91D/ZrO_2 surface composite

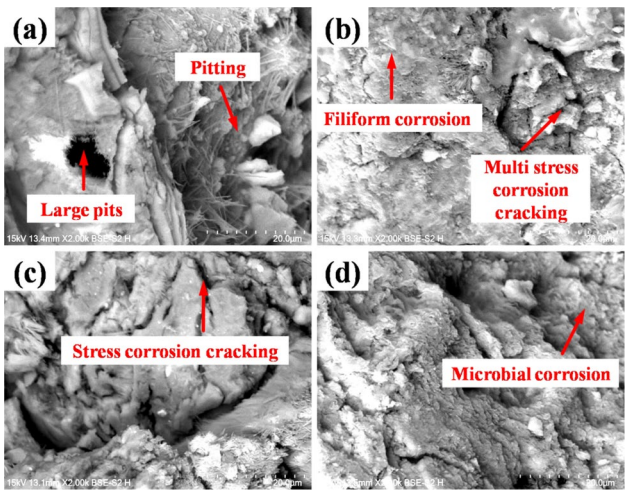

Fig. 24 Worn analysis after 15 days immersion. **a** AZ91D alloy, **b** AZ91D/Y_2O_3, **c** AZ91D/HA, and **d** AZ91D/ZrO_2 surface composite

and $Mg(OH)_2$ compounds [51].The significance of magnesium ions was released during immersion, which helped to produce more metallic phases due to the presence of HA particles. Thus, after 30 days immersion, corroded pits increased along with multi-directional crack propagations, as shown in Fig. 25c. Due to the fact that the fragmented precipitate's fissures propagated into huge gaps, which could cause localized corrosion inside the precipitates [52, 53]. After 30 days of immersion, the surface was densely packed with precipitates of irregularly arranged globular, which reduced the corrosion rate. Hence, the increased apatite layer which revealed the enhanced bioactivity of HA-reinforced surface morphologies as compared to the Y_2O_3- and ZrO_2-reinforced FSP surface composite after 15 and 30 days immersion in SBF solution, as shown in Fig. 24b and d, as well as in Fig. 25b and d. The increased immersion days formed a thick apatite layer on the surface which exhibited a spherical morphology with decreased

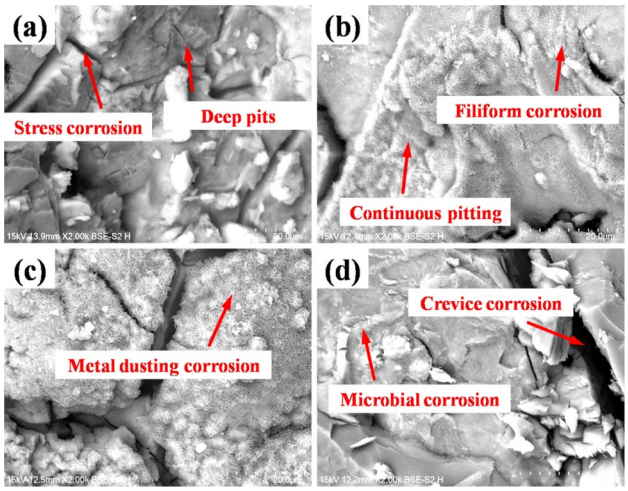

Fig. 25 Worn analysis after 30 days immersion. **a** AZ91D alloy, b AZ91D/Y_2O_3, **c** AZ91D/HA, and **d** AZ91D/ZrO_2 surface composite

stress corrosion and microbial corrosion feature due to presence of HA Particles into matrix [20].

Similarly, the ZrO_2-reinforced surface composite shows an increased mass loss after 30 days of immersion as compared to 7 and 15 days of immersion, but the mass loss is lower than that of the Y_2O_3- and HA-reinforced surfaces at three passes. This is because the worn features correspond to ZrO_2 dispersion and the accumulation of materials into the surface matrix. Meanwhile, better bioactivity behaviors are formed in apatite layers between the FSPed AZ91D/ZrO_2 surface and the composition of the SBF solution. The accumulated materials correspond to the well-known worn features during the degradation of $MgCO_3$, MgC_{l2}, and $Mg(OH)_2$. For the ZrO_2-reinforced surface, a localized corrosion phenomenon occurs only in a certain area of the FSP surface. Most of them remain adhered to the surface of the alloy for up to 30 days [20, 55]. The effect of the ZrO_2 particles is a reduced corrosion rate due to increased filiform and metal dusting corrosion features. The fragmented precipitates built-up size on the surface at 30 days was larger than that of the 7 and 15 days immersion. However, the FSP surface may present grains dislocation of large lateral dimensions, which might detach the grains and enhance the localized corrosion area after 30 days of immersion [56]. Also, the detached grain behaviors may be responsible for the crevice and microbial types' corrosion behavior.

4 Conclusions

The AZ91D/Y_2O_3, AZ91D/HA, and AZ91D/ZrO_2 FSPed surface composites were successfully fabricated through the friction stir processing technique. The comparative studies of the fabricated surface composites were investigated using microstructural analysis, microhardness, tensile strength, and corrosion tests. Based on comparative investigations, the conclusions are as follows:

- The average grain refinement of the AZ91D/Y_2O_3 (2.5 µm) was better than the AZ91D/HA (3.1 µm) and AZ91D/ZrO_2 (2.7 µm) FSPed surface composite at three passes by the strong dynamic recrystallization. The comparative recrystallized grains for the ZrO_2-reinforced composite and substructure grains for the Y_2O_3-reinforced composite were higher compared to others reinforced composites. While, the deformed grains were almost same for all reinforced composites
- The majority of the grains are refined with a peak basal texture {0001} < 11–20 > intensity for the Y_2O_3- (67.99), HA- (59.16), and ZrO_2- (89.45) reinforced composite. The inverse pole figures show a high intensity at < 11–20 > direction parallel to the processing direction. Hence, peak texture intensity as compared to the ZrO_2-reinforced surface decreased by 21.46 and 30.29 for the Y_2O_3- and HA-reinforced surfaces.
- At three passes, the microhardness values of the AZ91D/ZrO_2 (124 Hv) composite were significantly enhanced compared to the AZ91D/Y_2O_3 (115 Hv) and AZ91D/HA (111 Hv) composites due to better grain refinement and increased strengthening of the grain boundary. Similarly, the AZ91D/ZrO_2 surface composite exhibited a slightly enhanced UTS (159.1 MPa) compared to the AZ91D/Y_2O_3 and AZ91D/HA composite UTS (157.6 MPa) and (132.2 MPa).
- The corrosion resistance of the AZ91D/ZrO_2 composite for 30 days immersion was increased due to the domino effects and better bio-mineralization with the addition of ZrO_2 particles. While the AZ91D/Y_2O_3 and AZ91D/HA composites showed slightly decreased corrosion resistance. The typical worn surface revealed reduced deep pits and pitting, and cracks due to better generation of ionization of the hydrogen generated during immersion.

Author contribution Surendra Kumar Patel: roles/writing—original draft, conceptualization, data curation, formal analysis, investigation, methodology, and visualization; Guoxin Dai: writing—review and editing, data curation, validation, visualization, investigation, and conceptualization; Lei Shi: writing—review and editing, supervision, data curation, formal analysis, investigation, methodology, visualization, conceptualization, and funding acquisition; Chuansong Wu: writing—review and editing and conceptualization; Sergey Mironov: writing—review and editing and conceptualization; Lei Guan: writing—review and editing and conceptualization.

Funding The authors would like to acknowledge the financial support from the Shandong Provincial Science Foundation for Outstanding Young Scholars (Grant No. ZR2024YQ020), the National Natural

Science Foundation of China (Grant Nos. 52275349 and 52035005), the Key Research and Development Program of Shandong Province (Grant No. 2021ZLGX01), and the Natural Science Foundation of Guangdong Province (Grant No. 2023A1515012655). The research was also sponsored by the China/Shandong University International Postdoctoral Exchange Program.

Data availability The processed data required to reproduce these findings cannot be shared at this time as the data also forms part of an ongoing study.

Declarations

Competing interests The authors declare no competing interests.

References

1. Chai F, Zhang D, Li Y (2015) Microstructures and tensile properties of submerged friction stir processed AZ91 magnesium alloy. J Magnes Alloy 3(3):203–209. https://doi.org/10.1016/j.jma.2015.08.001
2. Gao L, Chen RS, Han EH (2009) Effects of rare-earth elements Gd and Y on the solid solution strengthening of Mg alloys. J Alloy Compd 481(1–2):379–384. https://doi.org/10.1016/j.jallcom.2009.02.131
3. Imandoust A, Barrett CD, Oppedal AL, Whittington WR, Paudel Y, Kadiri HE (2017) Nucleation and preferential growth mechanism of recrystallization texture in high purity binary magnesium-rare earth alloys. Acta Mater 138:27–41. https://doi.org/10.1016/j.actamat.2017.07.038
4. Zha M, Ma X, Jia H, Hua Z, Fan Z, Yang Z, Gao Y, Wang H (2023) Dynamic precipitation and deformation behaviors of a bimodal-grained WE43 alloy with enhanced mechanical properties. Int J Plast 168:103682. https://doi.org/10.1016/j.ijplas.2023.103682
5. Yang Y, Xiong X, Chen J, Peng X, Chen D, Pan F (2023) Research advances of magnesium and magnesium alloys worldwide in 2022. J Magnes Alloy 11(8):2611–2654. https://doi.org/10.1016/j.jma.2023.07.011
6. Ma X, Zha M, Wang S, Yang Y, Jia H, Gao D, Wang C, Wang H (2022) A rolled Mg−8Al−0.5Zn−0.8Ce alloy with high strength-ductility synergy via engineering high-density low angle boundaries. J Magnes Alloy 10(10):2889–2900. https://doi.org/10.1016/j.jma.2021.12.008
7. Ma A, Jiang J, Saito N, Shigematsu I, Yuan Y, Yang D, Nishida Y (2009) Improving both strength and ductility of a Mg alloy through a large number of ECAP passes. Mater Sci Eng A513–514:122–127. https://doi.org/10.1016/j.msea.2009.01.040
8. Sun Y, Yang C, Zhang B, Fan J, Li H, Zhao T, Li J (2023) The aging behavior, microstructure and mechanical properties of AlN/AZ91 composite. J Magnes Alloy 11(7):2458–2468. https://doi.org/10.1016/j.jma.2022.01.009
9. Barrett CD, Imandoust A, Kadiri AE (2018) The effect of rare earth element segregation on grain boundary energy and mobility in magnesium and ensuing texture weakening. Scr Mater 146:46–50. https://doi.org/10.1016/j.scriptamat.2017.11.004
10. Alemdar ASA, Jalal SR, Mulapeer MM (2023) Effect of exfoliation corrosion on the efficient hybrid joint of AA2024-T3 and AA2198-T8 formed by friction stir welding. Heliyon 9(6):e16577. https://doi.org/10.1016/j.heliyon.2023.e16577
11. Alemdar ASA, Jalal SR, Mulapeer MM (2022) Influence of friction stir welding process on the mechanical characteristics of the hybrid joints AA2198-T8 to AA2024-T3. https://doi.org/10.1155/2022/7055446.
12. Hou W, Ding Y, Huang G, Huda N, Shah LHA, Piao Z, Shen Y, Shen Z, Gerlich A (2022) The role of pin eccentricity in friction stir welding of Al-Mg-Si alloy sheets: microstructural evolution and mechanical properties. Int J Adv Manuf Technol 121:7661–7675. https://doi.org/10.1007/s00170-022-09793-x
13. Davis R, Singh A, Jackson MJ, Coelho RT, Prakash D, Charalambous CP, Ahmed W, Rosa L, Silva R, Lawrence AA (2022) A comprehensive review on metallic implant biomaterials and their subtractive manufacturing. Int J Adv Manuf Technol 120:1473–1530. https://doi.org/10.1007/s00170-022-08770-8
14. Zhu N, Sun C, Qian L, Wang M, Li X (2022) Novel process combined extrusion and severe plastic deformation for plate component with rib-web structure of magnesium alloys. Int J Adv Manuf Technol 119:3647–3658. https://doi.org/10.1007/s00170-021-08609-8
15. Ghorbani A, Zarei-Hanzaki A, Nezhadfar PD, Maghsoudi MH (2019) Microstructural evolution and room temperature mechanical properties of AZ31 alloy processed through hot constrained compression. Int J Adv Manuf Technol 102:2307–2317. https://doi.org/10.1007/s00170-019-03321-0
16. Arokiasamy S, Ronald BA (2017) Experimental investigations on the enhancement of mechanical properties of magnesium-based hybrid metal matrix composites through friction stir processing. Int J Adv Manuf Technol 93:493–503. https://doi.org/10.1007/s00170-017-0221-5
17. Khan I, Hussain G, Tariq M, Ilyas M (2018) Fabrication of UHMW polyethylene/nano-hydroxyapatite biocomposite via heat-assisted friction stir processing. Int J Adv Manuf Technol 96:3651–3663. https://doi.org/10.1007/s00170-018-1816-1
18. Mashtalyar DV, Imshinetskiy IM, Nadaraia KV, Gnedenkov AS, Sinebryukhov SL, Ustinov AY, Samokhin AV, Gnedenkov SV (2022) Influence of ZrO_2/SiO_2 nanomaterial incorporation on the properties of PEO layers on Mg-Mn-Ce alloy. J Magnes Alloy 10(2):513–526. https://doi.org/10.1016/j.jma.2021.04.013
19. Huang CA, Lin CK, Yeh YH (2010) Increasing the wear and corrosion resistance of magnesium alloy (AZ91D) with electrodeposition from eco-friendly copper- and trivalent chromium-plating baths. Surf Coat Tech 205(1):139–145. https://doi.org/10.1016/j.surfcoat.2010.06.012
20. Long F, Chen G, Zhou M, Shi Q, Liu Q (2023) Simultaneous enhancement of mechanical properties and corrosion resistance of as-cast Mg-5Zn via microstructural modification by friction stir processing. J Magnes Alloy 11(6):1931–1943. https://doi.org/10.1016/j.jma.2021.08.029
21. Millán-Ramos B, Morquecho-Marín D, Silva-Bermudez P, Ramírez-Ortega D, Depablos-Rivera O, García-López J, Fernández-Lizárraga M, Victoria-Hernández J, Letzig D, Almaguer-Flores A, Rodil S (2021) Biocompatibility and electrochemical evaluation of ZrO2 thin films deposited by reactive magnetron sputtering on MgZnCa alloy. J Magnes Alloy 9(6):2019–2038. https://doi.org/10.1016/j.jma.2021.07.010
22. Sathish T, Kamaraj L, Mohanavel V, Jazaa Y, Qahtani F, Althahban S (2023)A novel technique implementation to fabricate and analysis of AZ91D with TiN through FSP. Int J Adv Manuf Technol. https://doi.org/10.1007/s00170-023-12024-6.
23. Hou R, Victoria-Hernandez J, Jiang P, Willumeit-Römer R, Luthringer-Feyerabend B, Yi S, Feyerabend F (2019) In vitro evaluation of the ZX11 magnesium alloy as potential bone plate: Degradability and mechanical integrity. Acta Biomater 97:608–622
24. Sekar P, Panigrahi SK (2024) Understanding the corrosion and bio-corrosion behaviour of magnesium composites-a critical review. J Magnes Alloy 12(3):890–939. https://doi.org/10.1016/j.jma.2024.02.014

25. Thanikodi S, Giri J, Ramesh PT, Jagadeesan AK, Saravanan R (2024) Optimization of friction stir processing to improve the mechanical properties of bone fixation plate inputs made of ZK60 magnesium alloy. Int J Adv Manuf Technol. https://doi.org/10.1007/s00170-024-14002-y
26. Qin D, Shen H, Shen Z, Chen H, Fu L (2018) Manufacture of biodegradable magnesium alloy by high speed friction stir processing. J Manuf Process 36:22–32. https://doi.org/10.1016/j.jmapro.2018.09.019
27. Pei R, Zou Y, Zubair M, Wei D, Al-Samman T (2022) Synergistic effect of Y and Ca addition on the texture modification in AZ31B magnesium alloy. Acta Mater 233:117990. https://doi.org/10.1016/j.actamat.2022.117990
28. Abbasi M, Bagheri B, Dadaei M, Omidvar HR, Rezaei M (2015) The effect of FSP on mechanical, tribological, and corrosion behavior of composite layer developed on magnesium AZ91 alloy surface. Int J Adv Manuf Technol 77:2051–2058. https://doi.org/10.1007/s00170-014-6577-x
29. Asadi P, Givi MKB, Akbari M (2016) Simulation of dynamic recrystallization process during friction stir welding of AZ91 magnesium alloy. Int J Adv Manuf Technol 83:301–311. https://doi.org/10.1007/s00170-015-7595-z
30. Bahmani A, Arthanari S, Shin KS (2019) Improved corrosion resistant and strength of a magnesium alloy using multi-directional forging (MDF). Int J Adv Manuf Technol 105:785–797. https://doi.org/10.1007/s00170-019-04176-1
31. Zhang A, Lenin P, Zeng R, Kannan MB (2022) Advances in hydroxyapatite coatings on biodegradable magnesium and its alloys. J Magnes Alloy 10(5):1154–1170. https://doi.org/10.1016/j.jma.2022.01.001
32. Li H, Paidar M, Ojo OO, Vignesh RV, Iswandi I, Mehrez S, Zain AM, Mohanavel V (2023) Effect of tool profile on wear and mechanical behaviors of CeO2 and ZrO2-reinforced hybrid magnesium matrix composite developed via FSP technique. J Manuf Process 94:297–315. https://doi.org/10.1016/j.jmapro.2023.03.038
33. Zhen Y, Shen J, Hu S, Yin C, Yin F, Bu X (2022) Effect of rotation rate on microstructure and mechanical properties of CMT cladding layer of AZ91 magnesium alloy fabricated by friction stir processing. J Manuf Process 79:553–561. https://doi.org/10.1016/j.jmapro.2022.05.017
34. Zhao D, Ma X, Srivastava A, Turner G, Karaman I, Xie KY (2021) Significant disparity of non-basal dislocation activities in hot-rolled highly-textured Mg and Mg-3Al-1Zn alloy under tension. Acta Mater 207:116691. https://doi.org/10.1016/j.actamat.2021.116691
35. Zhao LY, Yan H, Chen RS, Han E (2021) The preferential growth and related textural evolution during static recrystallization in a cold-rolled Mg–Zn–Gd alloy. J Magnes Alloy 9(3):818–828. https://doi.org/10.1016/j.jma.2020.02.026
36. Bhattacharyya JJ, Agnew SR, Muralidharan G (2015) Texture enhancement during grain growth of magnesium alloy AZ31B. Acta Mater 86:80–94. https://doi.org/10.1016/j.actamat.2014.12.009
37. Liu Z, Cai Y, Chen J, Han J, Mao Z, Chen M (2021) Fabrication and characterization of friction stir–processed Mg-Zn-Ca biomaterials strengthened with MgO particles. Int J Adv Manuf Technol 117:919–932. https://doi.org/10.1007/s00170-021-07814-9
38. Xie J, Chen X, Cao Y, Huang G, Liu Q (2022) The evolution of main textures and the formation of P orientation with nanoprecipitates after friction stir processing. J Manuf Process 80:591–599. https://doi.org/10.1016/j.jmapro.2022.06.033
39. Zeng ZR, Zhu YM, Xu SW, Bian MZ, Davies CHJ, Birbilis N, Nie JF (2016) Texture evolution during static recrystallization of cold-rolled magnesium alloys. Acta Mater 105:479–494. https://doi.org/10.1016/j.actamat.2015.12.045
40. Ye X, Suo Z, Heng Z, Chen B, Wei Q, Umeda J, Kondoh K, Shen J (2024) An in-situ study of static recrystallization in Mg using high temperature EBSD. J Magnes Alloy 12(4):1419–1430. https://doi.org/10.1016/j.jma.2023.01.021
41. Li B, Liao M, Ma Q, McClelland Z (2015) Structure of grain boundaries with 30° [0001] misorientation in dynamically recrystallized magnesium alloys. Comp Mater Sci 101:175–180. https://doi.org/10.1016/j.commatsci.2015.01.034
42. Steiner MA, Bhattacharyya JJ, Agnew SR (2015) The origin and enhancement of {0001}〈112¯0〉 texture during heat treatment of rolled AZ31B magnesium alloys. Acta Mater 95:443–455. https://doi.org/10.1016/j.actamat.2015.04.043
43. Guo F, Pei R, Jiang L, Zhang D, Korte-Kerzel S, Al-Samman T (2020) The role of recrystallization and grain growth in optimizing the sheet texture of magnesium alloys with calcium addition during annealing. J Magnes Alloy 8(1):252–268. https://doi.org/10.1016/j.jma.2019.07.010
44. Balamurugan KG, Mahadevan K (2013) Investigation on the changes effected by tool profile on mechanical and tribological properties of friction stir processed AZ31B magnesium alloy. J Manuf Process 15(4):659–665. https://doi.org/10.1016/j.jmapro.2013.04.001
45. Iwaszko J, Kudła K (2021) Microstructure, hardness, and wear resistance of AZ91 magnesium alloy produced by friction stir processing with air-cooling. Int J Adv Manuf Technol 116:1309–1323. https://doi.org/10.1007/s00170-021-07474-9
46. Maqbool A, Lone NF, Ahmad T, Khan NZ, Siddiquee AN (2023) Effect of hybrid reinforcement and number of passes on microstructure, mechanical and corrosion behavior of WE43 Mg alloy based metal matrix composite. J Manuf Process 89:170–181. https://doi.org/10.1016/j.jmapro.2023.01.070
47. Das AK, Kumar R (2024) Investigation on wear behaviour of TiC/Co/Y2O3 metal matrix composite coating developed on AZ91D Mg alloy by plasma transferred arc cladding process. Mater Lett 255:135457. https://doi.org/10.1016/j.matlet.2023.135457
48. Kundu S, Thakur L (2023) An investigation on the fabrication and characterization of friction stir processed nano-HAp reinforced AZ91D magnesium matrix surface composite for bio-implants. J Mech Behav Biomed Mater 143:105918. https://doi.org/10.1016/j.jmbbm.2023.105918
49. Xu N, Feng R, Song Q, Zhao J, Bao Y (2021) Influence of heterogeneous microstructures on the mechanical properties of low-temperature friction stir processed AZ91D Mg alloy. Mater Sci Eng A 809:141004. https://doi.org/10.1016/j.msea.2021.141004
50. Li RG, Li HR, Zhao DY, Dai YQ, Fang DQ, Zhang JH, Zong L, Sun J (2020) High strength commercial AZ91D alloy with a uniformly fine-grained structure processed by conventional extrusion. Mater Sci Eng A 780:139193. https://doi.org/10.1016/j.msea.2020.139193
51. Wu B, Ibrahim MZ, Raja S, Yusof F, Razak BA, Muhamad MRB, Huang R, Zhang Y, Badruddin IA, Hussien M, Kamangar S (2022) The influence of reinforcement particles friction stir processing on microstructure, mechanical properties, tribological and corrosion behaviors: a review. J Mater Res Technol 20:1940–1975. https://doi.org/10.1016/j.jmrt.2022.07.172
52. El-Sayed MM, Shash AY, El-Danaf EA, Abd-Rabou M, ElSherbiny MG (2023) Impact of multi-pass friction stir alloying on the characterization of Mg based bio-ceramic nano composites. J Alloy Compd 959:170477. https://doi.org/10.1016/j.jallcom.2023.170477
53. Kumar K, Das A, Prasad SB (2023) Effect of multi-pass friction stir processing on mechanical, microstructural, bioactivity, and corrosion properties of novel magnesium-hopeite composite for biomedical applications. Mater Today Commun 35:105584. https://doi.org/10.1016/j.mtcomm.2023.105584

54. Fen-jun LIU, Yan JI, Yan-xia BAI (2020) Influence of multi-pass high rotating speed friction stir processing on microstructure evolution, corrosion behavior and mechanical properties of stirred zone on AZ31 allo. Trans Nonferrous Met Soc China 30(12):3263–3273. https://doi.org/10.1016/S1003-6326(20)65459-0
55. Rokkala U, Bontha S, Ramesh MR, Balla VK, Srinivasan A, Kailas SV (2021) Tailoring surface characteristics of bioabsorbable Mg-Zn-Dy alloy using friction stir processing for improved wettability and degradation behavior. J Mater Res Technol 12:1530–1542. https://doi.org/10.1016/j.jmrt.2021.03.057
56. Sunil BR, Kumar TSS, Chakkingal U, Nandakumar V, Doble M (2014) Friction stir processing of magnesium–nanohydroxyapatite composites with controlled in vitro degradation behavior. Mater Sci Eng C 39:315–324. https://doi.org/10.1016/j.msec.2014.03.004